A common human *MLKL* polymorphism confers resistance to negative regulation by phosphorylation

Sarah E. Garnish[1 2], Katherine R. Martin[1 2], Maria Kauppi[1 2], Victoria Jackson[1], Rebecca Ambrose[3 4], Vik Ven Eng[3 5], Daniel Frank[1], Emma C. Tovey Crutchfield[1 6], Komal M. Patel[1], Shene Chiou[1 2], Andre L. Samson[1 2], Marcel Doerflinger[1 2], Christopher R. Horne[1 2], Cathrine Hall[1], Samuel N. Young[1], Vicki Athanasopoulos[7], Carola G. Vinuesa[7], Charlotte A. Slade[1 2 8], Jaclyn S. Pearson[3 4 5], Gregor Ebert[9], John Silke[1 2], James M. Murphy[1 2] and Joanne M. Hildebrand[1 2 10]

1. The Walter and Eliza Hall Institute, Parkville, VIC, 3052, Australia
2. University of Melbourne, Department of Medical Biology, Parkville, 3052, Australia
3. Centre for Innate Immunity and Infectious Diseases, Hudson Institute of Medical Research, Clayton, VIC, 3168, Australia
4. Department of Molecular and Translational Science, Monash University, Clayton, VIC, 3168, Australia
5. Department of Microbiology, Monash University, Clayton, 3168, VIC, Australia
6. University of Melbourne, Faculty of Medicine, Dentistry and Health Sciences, Parkville, 3052, Australia
7. Department of Immunology and Infection, John Curtin School of Medical Research, Australian National University, ACT, Australia
8. Department of Clinical Immunology & Allergy, Royal Melbourne Hospital, Parkville, VIC, 3052, Australia
9. Institute of Virology, Technical University of Munich/Helmholtz Munich, Munich, Germany

10. To whom correspondence may be addressed- jhildebrand@wehi.edu.au

ABSTRACT

Across the globe, 2-3% of humans carry the *p.Ser132Pro* single nucleotide polymorphism in *MLKL*, the terminal effector protein of the inflammatory form of programmed cell death, necroptosis. We show that this substitution confers a gain in necroptotic function in human cells, with more rapid accumulation of activated $MLKL^{S132P}$ in biological membranes and $MLKL^{S132P}$ overriding pharmacological and endogenous inhibition of MLKL. In mouse cells, the equivalent *Mlkl S131P* mutation confers a gene dosage dependent reduction in sensitivity to TNF-induced necroptosis in both hematopoietic and non-hematopoietic cells, but enhanced sensitivity to IFN-β induced death in non-hematopoietic cells. *In vivo*, $Mlkl^{S131P}$ homozygosity reduces the capacity to clear *Salmonella* from major organs and retards recovery of hematopoietic stem cells. Thus, by dysregulating necroptosis, the S131P substitution impairs the return to homeostasis after systemic challenge. Present day carriers of the *MLKL S132P* polymorphism may be the key to understanding how MLKL and necroptosis modulate the progression of complex polygenic human disease.

INTRODUCTION

Necroptosis is a caspase independent form of programmed cell death that originated as a defense against pathogens (Kitur et al., 2016; Liu et al., 2021b; Pearson et al., 2017; Petrie et al., 2019; Upton et al., 2010). Highly inflammatory in nature, necroptosis results in the permeabilization of biological membranes and the release of cytokines, nucleic acids, and intracellular proteins into the extracellular space (Weir et al., 2021) Necroptosis is induced by danger- or pathogen-associated molecular patterns that signal via transmembrane receptors or intracellular pattern recognition receptors (He et al., 2011; He et al., 2009; Holler et al., 2000; Kaiser et al., 2013; Thapa et al., 2013). Of the various initiating stimuli, the most well studied necroptotic pathway is downstream of tumor necrosis factor receptor 1 (TNFR1)(Samson et al., 2021). In physiological contexts that favor low cellular inhibitor of apoptosis protein 1 (cIAP1) and caspase-8 activity, TNFR1 signals culminate in the formation of a high molecular weight platform called the necrosome that is nucleated by heterooligomeric RIPK1 and RIPK3 (Li et al., 2012; Meng et al., 2021; Mompean et al., 2018). Here, the terminal executioner protein, MLKL, is phosphorylated and activated by its upstream kinase, RIPK3 (Murphy et al., 2013; Sun et al., 2012; Zhao et al., 2012). Following phosphorylation, MLKL dissociates from RIPK3, oligomerizes and is trafficked to biological membranes where it interacts with Phosphatidylinositol Phosphates, or ‘PIPs’ (Cai et al., 2014; Chen et al., 2014; Dondelinger et al., 2014; Garnish et al., 2021; Hildebrand et al., 2014; Petrie et al., 2020; Samson et al., 2020; Sethi et al., 2022; Tanzer et al., 2016; Wang et al., 2014b). In human cells, association of activated MLKL oligomers with biological membranes can be inhibited by the synthetic compound necrosulfonamide (Samson et al., 2020; Sun et al., 2012; Wang et al., 2014a) or inhibitory phosphorylation of MLKL at Serine 83 (Zhu et al., 2022).

Pharmacological or mutation driven disruption at any major necroptotic signaling checkpoint compromises a cell's capacity to execute necroptosis.

In mouse studies, MLKL mediated cell death has been implicated as a driver or suppressor of diseases spanning almost all physiological systems depending on the pathophysiological context. The generation of *Mlkl* gene knockout (*Mlkl*$^{-/-}$), knock-in and conditional knock-out mouse models have enabled the role of necroptosis in infectious and non-infectious challenges to be dissected in physiological detail (Tovey Crutchfield et al., 2021). Interestingly, genetic deletion of *Mlkl* has no overt developmental or homeostatic effects in mice (Murphy et al., 2013; Wu et al., 2013). This is in direct contrast with two mouse models harboring *Mlkl* point mutations, *Mlkl*^{D139V} and *Mlkl*^{S83G}, that dysregulate MLKL activation, which results in early neonatal death and severe inflammatory phenotypes (Hildebrand et al., 2020; Zhu et al., 2022). Altogether, these observations suggest that while constitutive absence of MLKL-mediated death is benign, imbalanced execution of necroptotic cell death is deleterious.

Consistent with this notion, more than 20 unique disease-associated human germline gene variants in the core necroptotic machinery, encompassing *RIPK1*, *RIPK3*, *MLKL*, have been identified (Garnish and Hildebrand, 2022; Zhang et al., 2021). In one family, a haplotype including a rare *MLKL* loss-of-function gene variant (*p.Asp369GlufsTer22*, rs561839347) is associated with a severe and progressive novel neurogenerative spectrum disorder characterized by global brain atrophy (Faergeman et al., 2020). A more frequent *MLKL* loss-of-function gene variant (*p.Gln48Ter*, rs763812068) was found to be >20 fold enriched in a cohort of Hong Kong Chinese patients suffering from Alzheimer's disease (Wang et al., 2018) and common variants that cluster around the MLKL brace region were shown to be enriched *in trans* in a cohort of chronic recurrent multifocal osteomyelitis patients (Hildebrand et al., 2020). More recently, a hypomorphic *MLKL*

missense gene variant (*p.G316D*, rs375490660) was reported to be associated with Maturity Onset Diabetes of the Young (Hildebrand et al., 2021).

Here we present the cellular and physiological characterization of a serine to proline missense polymorphism at MLKL amino acid 132 (*p.Ser132Pro*; *S132P*). The *S132P* polymorphism is the third most frequent human *MLKL* missense coding variant in the gnomAD database; a large repository of whole genome and exome sequence data from humans of diverse ancestry (Karczewski et al., 2020). To examine the potential human disease-causing effects of this *MLKL* variant, we exogenously expressed $MLKL^{S132P}$ in human cell lines and introduced the mouse counterpart variant ($Mlkl^{S131P}$) into a genetically modified mouse model, revealing that this polymorphism confers MLKL gain-of-function in a cell- and stimulus-dependent manner. This MLKL gain-of-function manifests in *in vivo* changes to the immune response, impaired bacterial clearance, and defective emergency hematopoiesis. These observed phenotypes provide important insights into how this highly frequent human *MLKL S132P* polymorphism may contribute to the progression of complex disease.

Results

Family members carrying the *p.Ser132Pro* polymorphism exhibit diverse inflammatory disease profiles.

With a global minor allele frequency (MAF) of 0.0138, the *MLKL S132P* (rs35589326) polymorphism is predicted to be carried by 2-3% of the human population. It has not been detected in individuals assigned East Asian ancestry, is rare in individuals of African or Latino/Admixed American ancestry and is carried by an estimated 6-7% of individuals of Ashkenazi Jewish

ancestry (MAF 0.0315) (www.gnomAD.com, June 2022) **(Figure 1A)**. Notably, Ser132 is conserved across species, such as mouse, chimpanzee, rat, bovine, and pig **(Figure 1B)**.

We identified two individuals who are heterozygous carriers of the *MLKL S132P* polymorphism in an Australian registry of patients suffering from immune related disease. Patient 1, a female of South American heritage, was diagnosed with SAPHO (synovitis, acne, pustulosis, hyperostosis, osteitis) syndrome (inheritance chart unavailable). Patient 2, a female of European heritage, was diagnosed with systemic IgG4 disease **(Figure 1C)**. Both patients have one or more immediate family members carrying the *MLKL S132P* polymorphism who were also diagnosed with inflammatory diseases in early adulthood. Following whole genome sequencing, Patient 1 was found to exhibit a region of loss of heterozygosity (5:96031569 – 5:96364063) which covers *CAST*, *ERAP1*, *ERAP2* and *LNPEP*. These genes have been previously associated with inflammatory disease (Cortes et al., 2013; Cortes et al., 2015; Evans et al., 2011; Huang et al., 2013; Kirino et al., 2013; Robinson et al., 2015; Strange et al., 2010; Tsoi et al., 2012; Yin et al., 2015). Patient 2 does not carry any other predicted pathogenic gene variants. Primary peripheral blood mononuclear cells (PBMCs) isolated from patient 2 showed reduced MLKL protein levels, accompanied by a nominal increase in pro-inflammatory cytokine production in response to the Toll-like receptor (TLR) agonists, lipopolysaccharide and poly I:C, relative to age and sex matched healthy donor PBMCs not carrying the *MLKL S132P* polymorphism (**Supplementary Figure 1A, B)**.

Exogenously expressed *MLKL^{S132P}* confers resistance to chemical and natural regulatory inhibition.

To examine any changes to MLKL function conferred by this common polymorphism, we stably transduced parental wild-type (WT) and *MLKL*$^{-/-}$ versions of the human colonic epithelial cell line HT29 with doxycycline inducible *MLKL*^{WT} and *MLKL* ^{S132P} gene expression constructs. We also included the T357/S358 phosphosite mutant *MLKL*^{TSEE}, previously shown to be inactive, as a negative control for necroptosis induction (Petrie et al., 2018). Cells expressing *MLKL*^{S132P} died with similar kinetics to *MLKL*^{WT} following necroptotic stimulation (TNF, SMAC mimetic compound A and pan-caspase inhibitor IDN-665; TSI) and, as expected, *MLKL*^{TSEE} reconstituted cells were resistant to necroptotic cell death **(Figure 1D, Supplementary Figure 1C, D**). Interestingly, in the presence of the MLKL inhibitor necrosulfonamide (NSA), TSI-stimulated cells expressing *MLKL*^{S132P} exhibited higher levels of cell death than their *MLKL*^{WT} counterparts at later timepoints **(Figure 1D, Supplementary Figure 1C)**. We termed this override of MLKL inhibition 'breakthrough' cell death. Breakthrough death also occurred when *MLKL*^{S132P} was co-expressed with endogenous *MLKL* and increased when MLKL expression was augmented by higher doses of doxycycline **(Figure 1D**, **Supplementary Figure 1C, D).** We also observed breakthrough death in both wild-type and *MLKL*$^{-/-}$ forms of the human monocytic cell line U937, indicating this is not a cell type specific phenomenon **(Supplementary Figure 1E, F)**. Breakthrough death was neither due to differences in MLKL expression, nor changes in MLKL phosphorylation (T357/S358), because both were equivalent between *MLKL*^{WT} and *MLKL*^{S132P} reconstituted cells **(Figure 1E, Supplementary Figure 1G, H)**. Instead, cellular fractionation experiments suggest that breakthrough death was likely due to enhanced association of MLKL^{S132P} with biological membranes **(Figure 1F, Supplementary Figure 1I)**.

The small molecule inhibitor, necrosulfonamide (NSA), blocks human MLKL activity through covalent modification of Cysteine 86, located in the MLKL four helix-bundle, executioner domain

(Figure 1G) (Sun et al., 2012; Wang et al., 2014a)**.** Recently, it was discovered that MLKL can be endogenously phosphorylated at the proximal residue, Ser83, and this phosphorylation event plays a species conserved inhibitory role in both human (Ser83) and mouse (Ser82) **(Figure 1G)** (Zhu et al., 2022). Like NSA, phosphorylation of MLKL Ser83 does not alter the capacity of RIPK3 to phosphorylate MLKL at Ser357/T358 but prevents necroptosis by blocking the association of MLKL with cellular membranes (Zhu et al., 2022). To test whether phosphorylation at Ser83 is, like NSA, less effective at inhibiting $MLKL^{S132P}$ induced death, we created stable HT29 ($MLKL^{-/-}$ and wild-type) cell lines that exogenously expressing gene constructs encoding $MLKL^{WT}$, $MLKL^{S132P}$, $MLKL^{S83D}$ (phosphomimetic) and double mutant $MLKL^{S83D,S132P}$. Consistent with recent studies, the phosphomimetic mutation of S83, $MLKL^{S83D}$, ablated the capacity of MLKL to execute necroptotic cell death (Zhu et al., 2022). Also, as previously reported, the inhibitory effect of $MLKL^{S83D}$ overrode the activating effects of endogenous MLKL phosphorylation at Ser357/Thr358 **(Figure 1H, Supplementary Figure 1J, K)**. Exogenous expression of $MLKL^{S83D}$ also reduced total levels of necroptotic cell death in the presence of endogenous MLKL, indicating that this S83 phosphomimetic acts in a dominant negative manner **(Supplementary Figure 1L)**. Strikingly, combining the $MLKL^{S132P}$ and $MLKL^{S83D}$ amino acid replacements to create the compound mutant $MLKL^{S83D,\ S132P}$ restored necroptotic cell death responsiveness, albeit with reduced kinetics and reduced maximal cell death when compared to $MLKL^{S132P}$ alone **(Figure 1H, Supplementary Figure 1K)**. The $MLKL^{S132P}$ variant also partially overcomes the dominant negative effect of Ser83 phosphomimetic mutation in a wild-type background **(Supplementary Figure 1L)**. These data suggest that necroptotic cell death is dysregulated in human carriers of the common *MLKL S132P* variant. This conclusion, together with the finding of immunoinflammatory

disorders in *MLKL S132P* carriers, raises important questions about how, when, and where, proper regulation of necroptosis contributes to immune function *in vivo.*

A mouse model of the human *MLKL S132P* polymorphism exhibits differences in steady state immune cell populations

To address if the *MLKL S132P* polymorphism contributes to immunoinflammatory disease, we performed detailed histological, immunophenotypic, and experimental analyses of a CRISPR generated knockin mouse which carried the orthologous mutation, *Mlkl*^{S131P}. *Mlkl*^{S131P} heterozygotes and homozygotes were born according to the expected Mendelian ratios and had normal lifespans **(Figure 2A, B)**. The healthy presentation of *Mlkl*^{S131P} mice contrasts with the lethal phenotypes of mice engineered to encode *Mlkl*^{D139V} and *Mlkl*^{S83G} mutations (Hildebrand et al., 2020; Zhu et al., 2022). Wild-type, *Mlkl*^{S131P} heterozygote and homozygote mice had comparable body weight and no gross histological differences up to 9 months of age **(Figure 2C, Supplementary Figure 2A)**. Notably different to *Mlkl*^{D139V} or *Mlkl*^{S83G} homozygotes, no inflammation was detected in the salivary glands, mediastinum, liver or lungs (**Supplementary Figure 2A)** (Hildebrand et al., 2020; Zhu et al., 2022). No differences in the number of circulating platelets, red blood cells, or white blood cells were observed between wild-type, *Mlkl*^{S131P} heterozygote and homozygote mice across age **(Supplementary Figure 2B-D)**. However, reduced numbers of classical Ly6C^{hi} 'inflammatory' monocytes in the bone marrow, but not in the secondary lymphoid organs (spleen and inguinal lymph nodes), were observed in *Mlkl*^{S131P} homozygotes relative to wild-type controls (**Figure 2D, Supplementary Figure 2E, K, Q)**. In the secondary lymphoid organs, *Mlkl*^{S131P} homozygotes had a small but significant increase splenic

CD4^{+} T cells and B cells relative to wild-type controls **(Figure 2E, Supplementary Figure 2N-P).** All other innate and adaptive immune cell populations were comparable between genotypes in the bone marrow, spleen, and inguinal lymph nodes **(Figure 2D-F, Supplementary Figure 2E-V)**.

We next sought to address whether mouse MLKL^{S131P} exhibited a gain-in-function consistent with what we described for MLKL^{S132P} in human cells. Primary and immortalized fibroblasts isolated from the dermis of *Mlkl*^{S131P} homozygote, heterozygote and wild-type mice were examined for their relative capacity to die in the presence or absence of death stimuli. We did not observe any differences in TNF-induced apoptosis (TNF and SMAC mimetic; TS) between *Mlkl*$^{S131P/S131P}$ and *Mlkl*$^{WT/WT}$ immortalized MDFs **(Figure 2G)**. However, *Mlkl*$^{S131P/S131P}$ MDFs showed a diminished capacity to undergo TSI-induced (TNF, SMAC-mimetic compound A, pan-caspase inhibitor IDN-6556; TSI) necroptotic cell death **(Figure 2G, Supplementary Figure 2W)**. This was driven by a gene-dosage reduction in MLKL protein level present in MDF cells with the *Mlkl*^{S131P} allele **(Figure 2H, Supplementary Figure 2X)**. Immortalized MDFs, and to a lesser extent primary MDFs, did show clear *Mlkl*^{S131P} gene-dose dependent sensitivity to IFN-β, a strong inducer of *Mlkl* gene expression in mice **(Figure 2G, Supplementary Figure 2W)** (Rodriguez et al., 2016). This sensitivity was further enhanced by TNF and was refractory to inhibitors of RIPK1 (Nec-1s) or RIPK3 (GSK-872) **(Figure 2G, Supplementary Figure 2W)**. These results are analogous to cells expressing the auto active MLKL^{D139V} mutant (Hildebrand et al., 2020) and together support the notion that MLKL^{S131P} has constitutive RIPK3-independent activity when endogenously expressed in mouse cells (Hildebrand et al., 2020). These endogenous *Mlkl*^{S131P} observations were not limited to fibroblasts. In bone marrow derived macrophages (BMDMs), *Mlkl*$^{S131P/S131P}$ cells also exhibited diminished sensitivity to TSI-induced necroptosis and endogenously produced MLKL^{S131P} was

present at reduced levels in comparison to MLKL^{WT} **(Supplementary Figure 2Y, Z)**. In contrast to immortalized dermal fibroblasts, BMDMs derived from *Mlkl*^{S131P} homozygotes did not undergo cell death in the presence of IFN-β alone, despite clear IFN-β induced upregulation of MLKL protein relative to untreated cells **(Supplementary Figure 2Y, Z)**. Overall, these data show that across different cell types MLKL^{S131P} is not toxic at steady state, but upon different stimuli, both gain-of-sensitivity and loss-of-sensitivity to necroptotic cell death is evident. This suggests that diseases caused by the *MLKL S132P* polymorphism are likely to be diverse, with cell- or context-specific manifestations.

Emergency hematopoiesis is defective in *Mlkl*$^{S131P/S131P}$ mice

Differences in steady state immune cell populations suggest that overt pathological phenotypes may develop in *Mlkl*^{S131P} homozygotes following experimental challenge. Specifically, reduced numbers of steady state Ly6C^{hi} monocytes in the bone marrow of *Mlkl*^{S131P} homozygotes could indicate a defect in hematopoiesis. To test this, we examined recovery from myelosuppressive irradiation as an assessment of hematopoietic function in mice carrying the *Mlkl*^{S131P} allele. Following myelosuppressive irradiation, recovery of hematopoietic cell numbers and circulating peripheral blood cells was significantly delayed in *Mlkl* $^{S131P/S131P}$ mice compared with wild-type controls (**Figure 3A-F)**. In *Mlkl*$^{S131P/S131P}$ mice, peripheral red blood cell and platelet numbers were significantly reduced at 14 days post irradiation, with the former also decreased at 21 days **(Figure 3A, B)**. Despite equivalent total white blood cell numbers at 21 days post irradiation, a significant reduction in peripheral monocyte numbers and a non-significant decrease trend in neutrophils was observed in *Mlkl* $^{S131P/S131P}$ mice compared to wild-type controls **(Figure 3C, Supplementary Figure 3A, B)**. These reductions in circulating blood cell numbers were accompanied by

significant decreases in the nucleated viable, progenitor, and LSK cell populations in the bone marrow of *Mlkl*$^{S131P/S131P}$ mice **(Figure 3D-F)**. Contrastingly, at 21 days post irradiation, *Mlkl* ^{S131P} heterozygotes displayed a significant increase in their total nucleated viable cells in comparison to wild-type controls. This was driven predominantly by significant increases in the number of LSK cells (**Figures 3D, E)**.

To investigate whether the *Mlkl*^{S131P} homozygote defect was intrinsic to the hematopoietic stem cells, we performed competitive transplantation studies. *Mlkl*$^{S131P/S131P}$ or *Mlkl*$^{WT/WT}$ bone marrow was mixed with GFP^{+} competitor bone marrow in a 50:50 ratio and injected into Ly5.1 irradiated hosts. Six weeks post-transplant, *Mlkl*$^{WT/WT}$ bone marrow had competed with GFP^{+} bone marrow effectively, whilst *Mlkl*$^{S131P/S131P}$ bone marrow performed poorly, contributing to 7%, 5% and 9% of PBMCs (Ly5^{+}), red blood cells and platelets respectively **(Figure 3G-I)**. Similarly, *Mlkl*$^{S131P/S131P}$ bone marrow was outcompeted, again contributing to less than 10 % of the blood cells, when mixed in excess at 70:30 with GFP^{+} competitor bone marrow **(Supplementary Figure 3C-E)**. Thus, the defect in emergency hematopoiesis was intrinsic to *Mlkl*$^{S131P/S131P}$ hematopoietic stem cells, consistent with the intrinsic defect previously reported for the *Mlkl*^{D139V} autoactivating mutant (Hildebrand et al., 2020).

Recruitment of Ly6C^{hi} monocytes to sites of sterile inflammation is reduced in *Mlkl*$^{S131P/S131P}$ mice

To examine if the defects in emergency hematopoiesis displayed by *Mlkl*$^{S131P/S131P}$ mice could result in defective immune cell recruitment to sites of inflammation or infection, we employed a model of localized sterile inflammation induced by zymosan. Intra-peritoneal injection of zymosan

results in a rapid influx of immune cells, predominantly neutrophils, into the peritoneal cavity over 72 hours (Martin et al., 2017). The cellular content of the peritoneal cavity and numbers of circulating peripheral blood cells was examined at 4- and 24-hours post zymosan injection. *Mlkl*$^{S131P/S131P}$ mice displayed equivalent early recruitment of neutrophils and other immune cells to the peritoneum **(Figure 4A, B, Supplementary Figure 4A-H).** However, at 24 hours post zymosan injection *Mlkl*$^{S131P/S131P}$ mice had significant reductions in the number of Ly6C^{hi} monocytes recruited to the peritoneum **(Figure 4C, D, Supplementary Figure 4I-P)**. In the peripheral blood, monocytes were significantly elevated in *Mlkl*$^{S131P/S131P}$ mice in comparison to wildtype controls at 4 hours post zymosan **(Figure 4E, Supplementary Figure 4Q-S)**. However, by 24 hours, the number of peripheral blood monocytes was equivalent between genotypes, with only a non-significant increase in neutrophils observed in *Mlkl*$^{S131P/S131P}$ mice **(Figure 4F, Supplementary Figure 4T-V)**. Compared to wild-type mice, the recruitment of Ly6C^{hi} monocytes to the peritoneum of *Mlkl*^{S131P} homozygotes was hampered. These decreases in Ly6C^{hi} monocytes at the site of sterile inflammation is likely to be driven by the reduced number of this population in the bone marrow at steady state.

We previously observed that *Mlkl*$^{S131P/S131P}$ cells exhibited reduced response to TSI-induced necroptosis. To assess whether this defect in necroptotic function was observed in activated immune cells recruited to sites of inflammation, we isolated neutrophils from the peritoneum at 4 hours post zymosan injection. Consistent with our previous *in vitro* findings, no differences were observed in the capacity of *Mlkl*$^{S131P/S131P}$ inflammatory neutrophils to undergo spontaneous apoptosis **(Figure 4G).** However, the percentage of *Mlkl*$^{S131P/S131P}$ inflammatory neutrophils dying following necroptotic stimulation, TSI, was decreased in comparison to wild-type neutrophils **(Figure 4H)**.

Mlkl^{S131P} homozygotes exhibit reduced capacity to clear *Salmonella* infection

Reductions in the recruitment of Ly6C^{hi} monocytes to sites of inflammation, raise important questions as to whether challenge with a pathogen may reveal defects in the immune cell response in *Mlkl*^{S131P} homozygotes. *Salmonella enterica* has long been an important pathogenic selective pressure in humans (Key et al., 2020). For non-typhoidal *Salmonella* serovars such as *S. enterica* serovar *Typhimurium*, human infection is typically limited to the gastric mucosa (Galan, 2021; Hohmann, 2001). In mice and immunocompromised humans, *S. Typhimurium* can cause severe systemic disease after dispersal from the gut by dendritic cells and macrophages to peripheral organs including the spleen and liver (Wemyss and Pearson, 2019).

Mlkl^{S131P} homozygote, heterozygote and wild-type mice were infected with a metabolically growth-attenuated *Salmonella typhimurium* strain BRD509 (from here referred to as *Salmonella),* via oral gavage (1 x 10^7 colony forming units (CFU)). Daily monitoring for the 14-day infection period showed no differences in core body temperature or body mass between genotypes **(Supplementary Figure 5A, B)**. Consistent with normal weights, there were no obvious differences in the integrity of the intestinal epithelial barrier or intestinal monocyte and macrophage populations at infection endpoint **(Figure 5A)**. Despite this, *Mlkl*$^{S131P/S131P}$ mice had increased *Salmonella* burden in both the spleen and liver compared to wild-type controls **(Figure 5B, Supplementary Figure 5C, D).** Bacterial colonization in the feces was increased in female *Mlkl*$^{S131P/S131P}$ mice relative to wild-type female controls **(Figure 5B, Supplementary Figure 5E)**. In the peripheral blood, *Mlkl*$^{S131P/S131P}$ mice had significantly reduced numbers of circulating lymphocytes and monocytes, as well as a trend towards decreased numbers of circulating

neutrophils **(Figure 5C, Supplementary Figure 5F-H)**. Infected *Mlkl*$^{S131P/S131P}$ mice also exhibited significant decreases in the quantity of splenic Ly6C^{hi} monocytes in comparison to infected wild-type controls **(Figure 5D, E, Supplementary Figure 5I-O)**. No differences in splenic Ly6C^{hi} monocytes were observed in uninfected mice, therefore the reduction in Ly6C^{hi} monocytes in infected spleens is likely to be due to the reduced number of this monocyte population in the bone marrow and defects in emergency monopoiesis. Furthermore, we did not observe any difference in the kinetics of *Salmonella* induced cell death in ex-vivo BMDM infection assays, nor inflammasome activation, measured by GSDMD cleavage **(Supplementary Figure 5P, Q)**. Together these data show a hindered pathogen defense in *Mlkl*^{S131P} homozygotes resulting from widespread immunophenotypic deficiencies. Combined, our investigations of *Mlkl*^{S131P} homozygotes under challenge highlight a defect in emergency hematopoiesis that manifests in a disruption to integral inflammatory and immune responses. This provides important insights into the potential causes of immunoinflammatory disorders in *MLKL S132P* carriers.

DISCUSSION

Present in 2-3% of the global population, the high frequency *MLKL S132P* polymorphism confers a gain-of-function to MLKL resulting in hematopoietic dysfunction and immune cell defects in a genetically modified mouse model. In human cells, MLKL^{S132P} was resistant to chemical inhibition by necrosulfonamide treatment and endogenous inhibitory phosphorylation at Ser83. A gain in necroptotic function was also observed when murine equivalent *Mlkl*^{S131P} was examined *in situ*, with fibroblasts exhibiting RIPK3-independent cell death in the presence of IFN-β. When subject to endogenous protein regulatory mechanisms, MLKL^{S131P} protein levels are

reduced, manifesting in a reduced capacity for necroptosis in fibroblasts and immune cells stimulated with TSI. Extensive characterization of the *Mlkl*^{S131P} mouse unveiled steady state decreases in the bone marrow pool of inflammatory Ly6C^{hi} monocytes, that manifested in reduced numbers at the site of sterile inflammation and bacterial infection. Specifically, under infection challenge, an increased burden of *Salmonella* was present in the spleen and liver of homozygotes, accompanied by significant reductions in the circulating lymphocytes and monocytes. We observed significant hematopoietic dysfunction in *Mlkl*^{S131P} homozygotes, with a catastrophic drop in emergency hematopoiesis and complete failure of hematopoietic stem cells under transplant. In sum, both the human *MLKL* ^{S132P} and mouse equivalent *Mlkl* ^{S131P} variants confer a gain-of-function to MLKL *in vitro*. The resultant dysregulation of necroptotic signaling manifests in debilitating deviations in baseline immune phenotype and function in our genetically modified mouse model, *Mlkl*^{S131P}.

Prior to this work two other single point mutant *Mlkl* mouse models, *Mlkl*^{D139V} and *Mlkl*^{S83G}, had been reported, both of which exhibited full or partial homozygous postnatal lethality characterized by severe inflammation (Hildebrand et al., 2020; Zhu et al., 2022). In stark contrast to these models, the *Mlkl*^{S131P} homozygotes were born normal and with no signs of inflammatory disease at steady state. However, upon challenge, similarities are observed between *Mlkl*^{S131P} and *Mlkl*^{D139V} mice. Hematopoietic dysfunction is observed following myelosuppressive irradiation in homozygous or heterozygous mice harboring the *Mlkl*^{S131P} or *Mlkl*^{D139V} mice respectively (Hildebrand et al., 2020).

Despite the ostensible basal state phenotypes of *Mlkl*^{D139V} (Hildebrand et al., 2020) and recently described *Mlkl*^{S83G} (Zhu et al., 2022) homozygotes differing from the *Mlkl*^{S131P} homozygotes, there were similarities observed at the molecular level. As for MLKL^{S131P}, RIPK3-

independent gain-of-function was reported for MLKL^{D139V}, but not MLKL^{S83G} (Hildebrand et al., 2020; Zhu et al., 2022). This major similarity in molecular function is not unexpected considering the proximity of the D139 and S131 residues within MLKL. Constitutive activity of both the S132P and D139V brace helix mutants is restrained by cellular mechanisms that limited protein level, with decreases in endogenous MLKL observed in cells generated from *Mlkl*^{S131P} and *Mlkl*^{D139V} homozygotes. Interestingly, ubiquitin-mediated targeting of MLKL to the lysosome was identified to be mechanistically involved in the restraint of necroptosis in cells expressing MLKL^{D139V}, and as a means of clearing endosomal *Listeria monocytogenes* and *Yersinia enterocolita* (Hildebrand et al., 2020; Liu et al., 2021a; Yoon et al., 2022). Exploring if the reduction in cellular MLKL levels we observed in the PBMCs of a human carrier of the *S132P* polymorphism, or cells isolated from the S131P mouse, is likewise mediated by ubiquitination and lysosomal targeting will be an important next step, particularly as it relates to the clearance of these intracellular bacteria from human cells. Ablation of the inhibitory phosphorylation site in *Mlkl*^{S83G} mice similarly subjects MLKL to downregulation in mouse cells (Zhu et al., 2022). In sum, our analysis of MLKL^{S131P} further highlights the importance of mechanisms that downregulate MLKL when aberrantly activated.

The finding that MLKL^{S132P} retains necroptotic killing activity despite simulated inhibitory phosphorylation at Ser83 in human cells is highly notable. The inflammatory phenotypes that result from homozygosity of phosphomimetic (S83G) mutation provides insight into the potential disease development that may occur in carriers of the *MLKL S132P* polymorphism under environmental and cellular scenarios where Ser83 inhibitory phosphorylation is deployed. Identifying the kinase(s) responsible for phosphorylation at MLKL Ser83 and understanding which cell types are primed to deploy this kinase(s) is an important next step in determining if this

polymorphism promotes clinically relevant changes to homeostasis or disease outcomes in humans.

Evidence for positive selection has been found for over 300 immune-related gene loci and many of these have been found to be associated with the incidence of autoimmune and autoinflammatory disease in modern humans (Gutierrez-Arcelus et al., 2016; Ramos et al., 2015). Many of these variants have also been mechanistically linked to defense against a particular pathogen (Karlsson et al., 2014, Ramos et al., 2015), with pathogenic microbes a major driver of genetic selection over human history. While a diminished capacity for mice to clear disseminated *Salmonella* would argue against the hypothesis that the *MLKL S132P* polymorphism has been positively selected for in human populations, it is important to note that only 1.4 % of human carriers are homozygotes (Karczewski et al., 2020). *MLKL S132P* heterozygosity is by far the most prevalent, and evolutionarily relevant, human scenario. *Mlkl*^{S131P} heterozygotes displayed gene dosage phenotypes consistent with homozygotes, with one exception. Following sublethal myelosuppressive irradiation, a gain in bone hematopoietic stem cell numbers in heterozygotes was observed whilst a catastrophic drop occurred in homozygotes. Whether this increase in stem cell numbers persists over time is currently under investigation. However, increased fitness conferred to heterozygous mice at this timepoint provides intriguing insights into other selective pressures that may have promoted accumulation of this polymorphism in humans (Werren et al., 2021). Sepsis, where emergency hematopoiesis is an essential determinant in survival, is an interesting and highly evolutionarily significant avenue of exploration for the study of *MLKL S132P* polymorphism frequency (Boomer et al., 2011; Brinkworth and Valizadegan, 2021). With nutrition being another important driver of genetic adaptation in humans, exploring the role of *MLKL S132P* in metabolic disease is also compelling. An important precedent for this is a recent

report of an association between human RIPK1 promoter polymorphisms and diet-induced obesity (Karunakaran et al., 2020). The potential for negative selection of this polymorphism over time is also an important avenue of exploration in light of the recent discovery of a common *TYK2* variant accounting for and its role in enhancing susceptibility to severe infection by historically important human pathogen mycobacterium tuberculosis (Boisson-Dupuis et al., 2018; Kerner et al., 2021).

By many, MLKL is viewed as a potential therapeutic target for drug discovery due to its established involvement in multiple human diseases, especially inflammatory pathologies (Hildebrand et al., 2020; Pierdomenico et al., 2014; Rickard et al., 2014a; Rickard et al., 2014b). To date no human clinical trials have been conducted on MLKL-targeted small molecules, although several inhibitors have been reported in the literature, including first-of-kind human MLKL inhibitor necrosulfonamide (NSA), which all function by targeting Cys86 (Sun et al., 2012; Yan et al., 2017). Intriguingly, we show that in the presence of NSA human $MLKL^{S132P}$ protein displays a gain-of-function that results in non-inhibitable cell death. While NSA has been a fundamental tool for *in vitro* studies of necroptosis, our findings raise serious questions about the suitability of Cys86 as a target for MLKL drug discovery programs, because such therapies would not be suitable for 2-3% of the population that carry the *MLKL S132P* polymorphism.

METHODS

Patient Recruitment, Ethics and Informed consent

Patients and their relatives were recruited from the Department of Clinical Immunology and Allergy, Royal Melbourne Hospital, Victoria, Australia and the Centre for Personalized Immunology, Australian National University, Canberra, Australia. Unrelated, age and sex matched

‘healthy’ controls that did not carry the *MLKL p.Ser132Pro* polymorphism were recruited via the Volunteer Blood Donor Registry, Parkville. Informed consent was obtained from all participants for genomic analysis and immunological studies. All procedures were performed and are reported here with the approval of human ethics review boards of all Institutes that participated in human genetics studies; Australian National University, The Walter and Eliza Hall Institute of Medical Research (approved projects 2009.162, 10/02) and with the 1964 Helsinki declaration and its later amendments or comparable ethical standards.

Genomic analysis

Whole exome sequencing was performed by the Canberra Clinical Genomics service. Libraries were prepared and enriched using the SureSelect Clinical Research Exome v2 kit (Agilent Technologies), and targeted regions were sequenced using an Illumina sequencing system with 100bp paired-end reads, with an average depth of >35. Reads were aligned to the human genome reference sequence (GRCh38) using the Burrows-Wheeler Aligner (BWA-MEM), and variant calls made using the Genomic Analysis Tool Kit (GATK).

Animal ethics

All mice were housed at the Walter and Eliza Hall Institute of Medical Research (WEHI), Australia. This facility is a temperature and humidity controlled specific pathogen free facility with a 12h:12h day night cycle. All experiments were approved by the WEHI Animal Ethics Committee in accordance with the Prevention of Cruelty to Animals Act (1986) and the Australian National Health and Medical Research Council Code of Practice for the Care and Use of Animals for Scientific Purposes (1997).

Mice

Mice were generated on a C57BL/6J background. The *p.Ser131Pro* mutation in the *Mlkl* gene (*Mlkl*^{S131P}) was generated using CRISPR/Cas9 by the Melbourne Advanced Genome Editing Centre (MAGEC) laboratory at WEHI, following the same methodology as previously described (Hildebrand et al., 2020; Wang et al., 2013). To introduce a proline-coding mutation in place of Ser131 within the *Mlkl* gene, an sgRNA of the sequence CTGTCGATCTTCCTGCTGCC was used to create double stranded breaks within the *Mlkl* locus and initiate homologous recombination.

An oligo donor (TGTTGCTGCTGCTTCAGGTTTATCATTGGAATACCGTTTCAGATGTCAGCCAGCCAGCACCATGGCAGCAGGAAGATCGACAGGATGCAGAGGAAGACGGgtgagtctcccaaagactggga) was subsequently used to introduce the S131P mutation. Genotyping of mice was completed by Transnetyx using custom probe Mlkl-8 MUT (Forward Primer: CTGCTTCAGGTTTATCATTGGAATACC, Reverse Primer: TCTGCATCCTGTCGATCTTCCT).

Reagents

Antibodies; Rat anti-mMLKL 8F6 (1:2000), rat anti-mMLKL 5A6 (1:1000), rat anti-hMLKL 10C2 (1:1000), rat anti-hMLKL 7G2 (1:1000), rat anti-hRIPK3 1H2 (1:1000) were produced in-house. Mouse anti-actin (A-1978; 1:5000) was purchased from Sigma-Aldrich, rabbit anti-GAPDH (#2118; 1:2000-5000) was purchased from Cell Signalling Technology, rabbit anti-VDAC (AB10527; 1:10000) was purchased from Millipore, rabbit anti-human pMLKL (EPR9514; 1:1000-3000) was purchased from Abcam, and rabbit anti-mouse pMLKL (D6E3G; 1:1000) was purchased from CST. Cell treatments were completed with agonists/antagonists at the following concentrations: 100 ng/ml recombinant hTNF-fc (produced in house as in (Bossen et

al., 2006)), 500 nM SMAC mimetic Compound A (provided by Tetralogic Pharmaceuticals; as in (Vince et al., 2007), 5 µM Pan-caspase inhibitor IDN-6556 (provided by Tetralogic Pharmaceuticals), 1 µM necrosulfonamide (NSA; Merck #480073), 5 µM necrostatin (Nec-1s; Merk #504297), 1 µM GSK-'872 (SynKinase #SYN-5481), 10-20 ng/ml lipopolysaccharide (LPS; Sigma #L2630), 25 µg/ml polyinosinic:polycytidylic (Poly I:C; Novus), 200 nM MG132 (Merck #474790), 2 nM PS341 (Sigma #504314), and 30 ng/ml mouse IFNβ (R&D Systems #8234-MB-010)

Generation of cell lines

Mutations were introduced into a human MLKL DNA template (from DNA2.0, CA) using oligonucleotide-directed PCR and sub-cloned into the pF TRE3G PGK puro vector(Murphy et al., 2013). Vector DNA was co-transfected into HEK293T cells with pVSVg and pCMV R8.2 helper plasmids to generate lentiviral particles. U937 (WT and *MLKL*$^{-/-}$) and HT29 (WT and *MLKL*$^{-/-}$) were then stably transduced with exogenous human MLKL ligated into pFTRE3G. Successfully transduced cells were selected using puromycin (2.5µg/mL; StemCell Technologies) using established procedures (Hildebrand et al., 2014; Murphy et al., 2013; Petrie et al., 2018). The following oligonucleotides were used for the assembly of constructs:

hMLKL^{S132P} fwd; 5′ GCCAAGGAGCGCCCTGGGCACAG3′

hMLKL^{S132P} rev; 5′ CTGTGCCCAGGGCGCTCCTTGGC 3′

hMLKL^{TSEE} fwd; 5′ GAGGAAAACACAGGAGGAAATGAGTTTGGGAAC 3′

hMLKL^{TSEE} rev; 5′ GTTCCCAAACTCATTTCCTCCTGTGTTTCCTC 3′

hMLKL^{S83A} fwd; 5′ GTTCAGCAATAGAGCCAATATCTGCAG 3′

hMLKL^{S83A} rev; 5′ CCTGCAGATATTGGCTCTATTGCTGAAC 3′

hMLKL^{S83D} fwd; 5′ GAAAAGTTCAGCAATAGAGACAATATCTGCAGGTTTC 3′

hMLKL^{S83D} rev; 5′ GAAACCTGCAGATATTGTCTCTATTGCTGAACTTTTC 3′

Primary mouse dermal fibroblasts (MDFs) were prepared from skin taken from the head and body of 1-day old mice. These MDFs were immortalised by stable lentiviral transduction with SV40 large T antigen. Bone marrow derived macrophages were generated from the long bones of adult mice and grown for 7 days in DMEM supplemented with 15% L929 cell supernatant.

Human blood (patient and healthy donor) was collected by collaborators via venipuncture at the Royal Melbourne Hospital. Collected blood was diluted with PBS and layered on an equal volume of Histopaque (density 1.077 g/ml) and centrifuged for 30 minutes, 700 x g at room temperature. The layer containing peripheral blood mononuclear cells (PBMCs) was harvested and washed with PBS, then frozen in FCS + 10 % DMSO and stored in liquid nitrogen.

Culture of cell lines

Primary MDFs, immortalised MDFs and HT29s were cultured in DMEM + 8% FCS. BMDMs were cultured in DMEM + 15% FCS + 20% L929. U937 and PBMCs were cultured in RPMI + 8% FCS. All cell lines were grown at 37 °C and 10% (v/v) CO_2.

Western blot

U937 cells were seeded into 48-well plates at 60,000 cells/well and induced for 3 hours with doxycycline (20 ng/mL, 100 ng/mL or 500 ng/mL) to stimulate MLKL expression. HT29 cells were seeded into 48-well plates at 45,000 cells/well and following 12-14 hours of cell adherence, cells were induced overnight with doxycycline (20 ng/mL, 100 ng/mL or 500 ng/mL) for

stimulation of MLKL expression. BMDMs were plated at 400,000 cells/well in a 24-well plate and MDFs (primary and immortalised) were plated at 30,000 cells/well in a 48-well plate. Cells were stimulated as indicated at described for 6 hours, except for BMDMs stimulated with LPS for 2 hours before addition of SMAC-mimetic Compound A for a further 4 hours. Human primary PBMCs were plated at 45,000 cells/well and stimulated for 4 hours. All cells were harvested in 2 x SDS Laemmli's lysis buffer, boiled at 100 °C for 10-15 min, and then resolved by 4-15% Tris-Glycine SDS-PAGE (Bio-Rad). Proteins were transferred to nitrocellulose or PVDF membrane and probed with antibodies as indicated.

IncuCyte analysis

Primary and immortalised MDFs were plated at 8,000 cells per well in a 96-well plate. BMDMs were plated at 150,000 cells per well on day 6 of culture in a 48-well plate. MDFs and BMDMs were left to settle overnight before stimulation. The next day MDFs and BMDMs were stimulated in culture media supplemented with propidium iodide. HT29 cells were plated at 45,000 cells per well in a 48-well plate and left to settle for 6 hours before overnight doxycycline pre-stimulation (20ng/mL, 100ng/mL or 500ng/mL). HT29 cells were stimulated in Phenol Red-free media supplemented with 2% FCS, 1mM Na pyruvate, 1mM L-GlutaMAX, SYTOX Green (Invitrogen, S7020) and either DRAQ5 (Thermofisher, #62251) (MLKL KO HT29) or SPY_620 (Spirochrome, SC401) (WT HT29).

U937 cells were plated at 60,000 cells per well in a 48-well plate and were induced with doxycycline (20ng/mL, 100ng/mL or 500ng/mL) for 3 hours. Cells were then stimulated in Phenol Red-free media supplemented with 2% FCS, 1mM Na pyruvate, 1mM L-GlutaMAX, SYTOX Green and either DRAQ5 (MLKL KO HT29) or SPY_620 (WT HT29).

Neutrophils isolated from the peritoneum at 4 hours post-zymosan injection were counted and plated at 60,000 cells/well in a 48-well plate. Plating media (RPMI + 8 % FCS) was supplemented with SYTOX Green and DRAQ5 dyes.

Images were taken every hour using IncuCyte SX5 or S3 imaging and cell death was quantified by number of dead cells (SYTOX Green or propidium iodide positive). Percentage values were quantified by number of dead cells out of total live cell number (DRAQ5 positive).

TNF ELISA

100,000 cells were stimulated with LPS (10ng/mL) or Poly I:C (2.5µg/mL) for 3 hours. PBMC supernatant cytokine content was measured by ELISA (R&D: STA00C) according to the manufacturer's instructions. The measurements were performed in technical triplicates.

Mouse histopathology

7–9-month-old mice were euthanized by CO_2 and fixed in 10 % buffered formalin. For the full body, 5-µm sagittal sections were taken at 300-µm intervals of all organs. Histopathologists Aira Nuguid and Tina Cardamome at the Australian Phenomics Network, Melbourne completed thorough examination of these sections.

Haematological analysis

Cardiac, submandibular or retro-orbital blood collected from mice at steady state (8-52 weeks old) or following challenge was placed into EDTA coated tubes. Blood cells were left undiluted or diluted 2- to 11-fold in DPBS for automated blood cell quantification using an ADVIA 2120i haematological analyser on the same day as harvest.

Mouse model of *Salmonella* infection

Mice used in this experiment were a mix of littermates and non-littermates aged 6-12 weeks, and wildtype mice that were littermates behaved equivalently to non-littermates. Mice were infected with *Salmonella enterica* serovar Typhimurium strain BRD509 (Strugnell et al., 1992) at 10^7 colony forming units (CFU) by oral gavage. Mice were harvested 14 days post-infection. Cardiac bleeds were taken, and blood populations analysed using an ADVIA hematology analyser. Liver, spleen, and faeces were harvested for enumeration of viable bacteria on nutrient agar. Organs from infected mice were weighed and homogenised in 2 mL (spleens), 5 mL (livers) or 1 mL (faeces) of PBS. Homogenates were serially diluted (in duplicate) in PBS and 10 µl drops plated out in duplicate onto LB agar (+ streptomycin) and incubated overnight at 37 ºC. CFU/mL was calculated per organ for each mouse and then standardised to CFU/organ based upon organ weight. A small portion (1/3) of the spleen was processed for flow cytometry analysis.

***In vitro Salmonella* infection**

In vitro infection of BMDMs with *Salmonella enterica* serovar Typhimurium strain SL1344 were performed as previously reported (Doerflinger et al., 2020). BMDMs on day 6 of differentiation were plated at 4 x 10^5 cells/well in a 6-well plate for western blot analyses or 5 x 10^4 cells/well in a 96-well plate for LDH assays. Cells were infected at MOI:25 for western blot or MOI:10 or 50 for LDH assays in antibiotic-free DMEM for denoted incubation times. For all experimental analyses, following 30-minute incubation, cells were washed and replaced in DMEM media supplemented with 50 µg/ml gentamycin to ensure growth inhibition of extracellular bacteria. BMDM cell death levels were measured as a percentage of LDH release using the Promega CytoTox 96 Non-Radioactive Cytotoxicity Assay (G1780), according to manufacturer's instructions.

Sublethal irradiation

Mice were irradiated with a 5.5 Gy sub-lethal dose of γ-irradiation and received neomycin (2 mg/mL) in the drinking water for 3 weeks. At 4 days post irradiation, a retro-orbital bleed was analysed via ADVIA hematology to confirm successful irradiation. Mice had submandibular bleeds analysed by ADVIA hematology and had long bones harvested for flow cytometry analysis at either 7-, 14- or 21-days post irradiation to assess stem cell capacity.

Hematopoietic stem cell transplants

Donor bone marrow were injected intravenously into recipient *C57BL/6-CD45*$^{ly5.1}$ mice following 11 Gy of γ-irradiation split over two equal doses. Recipient mice received neomycin (2 mg/mL) in the drinking water for 3 weeks. Long term capacity of stem cells was assessed by flow cytometric analysis of donor contribution to recipient mouse peripheral blood at 6 weeks.

Zymosan induced peritonitis

1 mg of zymosan A from *Saccharomyces cerevisiae* (Sigma-Aldrich) was intra-peritoneally injected into mice to induce sterile peritonitis. After 4 or 24 hours, mice were euthanized, cardiac bled and bone marrow collected. The peritoneal cavity was washed with 1 ml of cold PBS and cells within the lavage fluid were collected by centrifugation (300 x g, 5 minutes). Bone marrow and peritoneum immune cells were quantified by flow cytometry.

Flow cytometry

To analyse the innate and adaptive immune cells in peripheral blood, inguinal lymph nodes, spleen and bone marrow, isolated single cell suspensions were incubated with a combination of the following antibodies: CD4-BV421, CD8-PECy7, CD19-PerCPCy5.5, CD11b-BV510 or BV786, GR1-PE, CD45-Alexa700, Ly6G-V450 and Ly6C-APCCy7.

Splenic immune cells were analysed at 14-day post *Salmonella* infection and incubated with a combination of the following antibodies: CD4-BV421, CD8-PeCy7, CD19-PerCPCy5.5, CD11b-BV510 or BV786, CD64-PE, CD45-Alexa700, Ly6G-V450 and Ly6C-APCCy7.

To analyse the contribution of donor and competitor cells in transplanted recipients, blood cells were incubated with either CD41-APC (ThermoFisher) and Ter119-PE or Ly5.1-A700, Ly5.2-PE-Cy7, CD4-PE, CD8-PE, B220-BV650, Ly6C-APCCy7, Mac1-PerCPCy5.5. To analyse stem- and progenitor- cell compartment following sub-lethal irradiation, bone marrow cells were incubated with cKit-PerCPe710 (ThermoFisher), CD48-PECy7 (ThermoFisher), CD150-A647, Sca1-APCCy7 (ThermoFisher), B220-PE, CD19-PE, CD4-PE, CD8-PE, Gr1-PE. Finally, fluorogold (AAT Bioquest Cat#17514) was added for dead cell detection where appropriate.

Peritoneal and bone marrow immune cells at 4- or 24- hours post-zymosan injection were incubated with CD45-Alexa700, CD64-BV650, Ly6G-PE, Ly6C-APCCy7, F4/80-PerCPCy5.5, CD11b-BV510, CD8-PECy7, CD4-FITC, B220-APC and FC-blocker. Finally, propidium iodide (2 µg/mL, Sigma-Aldrich) was added for dead cell detection.

All cells were analysed on the Aurora Cytex flow cytometer. With exception of zymosan induced peritonitis experiments that used the Aurora Cytex automated volume calculator, cells were mixed with counting beads to quantify absolute cell numbers. Except where denoted, all flow cytometry antibodies were obtained from BD Biosciences.

Statistical analyses

All data points signify independent experimental repeats or biologically independent data points. All p values were calculated in Prism using the statistical test identified in figure legends. Asterisks signify that $p \leq 0.05$ (*), $p \leq 0.01$(**) or $p \leq 0.001$ (***).

FIGURE LEGENDS

Figure 1. MLKL^{S132P} executes cell death in the presence of necrosulfonamide or Ser83 inhibition.

(A) Minor allele frequency of *MLKL p.Ser132Pro* according to the gnomAD database, stratified by ancestry. **(B)** Sequence alignment of conserved serine in the MLKL orthologs across different species. **(C)** Family pedigree of patient 2, identified from Australian registry of patients suffering from immune related disease. Known diagnoses for family members are indicated. (**D)** MLKL^{WT} and MLKL^{S132P} reconstitute necroptotic signaling, but as expected control protein harboring activation loop phosphomimetic substitutions, MLKL^{TSEE}, did not. Human MLKL expression was induced in *MLKL$^{-/-}$* HT29 cells with 100 ng/ml doxycycline (Dox) and treated with necroptotic stimulus (TNF, SMAC mimetic, IDN-6556; TSI) in the presence or absence of MLKL inhibitor Necrosulfonamide (NSA; 1µM). Cell death was measured every hour for 24 hours by percentage of SYTOX Green positive cells quantified using IncuCyte SX5 live cell imaging. Independent cell lines were assayed in *n=3-9* experiments, with errors bars indicating the mean ± SEM. **(E)** Western blot analyses of whole cell lysates taken 3 h post TSI stimulation in the presence or absence of NSA from doxycycline (100 ng/ml) induced *MLKL$^{-/-}$* HT29 cells expressing *MLKL^{WT}* or *MLKL^{S132P}*. **(F)** High molecular weight phosphorylated MLKL^{S132P} is present at enhanced levels in crude membrane fractions following Blue-Native PAGE under TSI stimulation in the presence or absence of NSA. **(G)** Ser83 (red), Cys86 (purple) and Ser132 (gold) highlighted as spheres on cartoon representation of human MLKL. Four-helix bundle domain shown in green, brace helices shown in beige and pseudokinase domain shown in blue. Homology model is generated from the N-terminal domain NMR structure (PDB:2MSV) and the C-terminal pseudokinase domain crystal structure (PDB: 4MWI) of human MLKL, which were aligned using the full-length murine crystal

structure (PDB:4BTF) (Murphy et al., 2013; Murphy et al., 2014; Su et al., 2014). **(H)** *MLKL S132P* mutation reconstitutes necroptotic signaling in the presence of Ser83 inhibitory phosphorylation (MLKL^{S83D}). Human MLKL expression was induced in *MLKL*$^{-/-}$ HT29 cells with 100 ng/ml doxycycline (Dox) and treated with necroptotic stimulus (TNF, SMAC mimetic, IDN-6556; TSI) in the presence or absence of MLKL inhibitor Necrosulfonamide (NSA; 1µM). Cell death was measured every hour for 23 hours by percentage of SYTOX Green positive cells quantified using IncuCyte SX5 live cell imaging. Independent cell lines were assayed in *n=4* experiments, with errors bars indicating the mean ± SEM. **(E/F)** Blot images are representative of at least three independent experiments.

Figure 2. In mice, *Mlkl*^{S131P} homozygosity is tolerated but results in steady state immune cell population differences.

(A) Macroscopic appearance of *Mlkl*$^{WT/WT}$ and *Mlkl*$^{S131P/S131P}$ mice at 8-12 weeks of age. **(B)** *Mlkl*$^{S131P/S131P}$ mice are born according to Hardy-Weinberg equilibrium as observed in the distribution of genotypes from *Mlkl*$^{WT/S131P}$ heterozygous intercrosses. **(C)** Body weight of *Mlkl*$^{WT/WT}$, *Mlkl*$^{WT/S131P}$ and *Mlkl*$^{S131P/S131P}$ mice at 3-4 or 7-9 months of age. Each dot represents an individual mouse (*n= 8-17*, mean ± SEM). **(D-F)** Flow cytometry quantification of innate (Ly6C^{hi} monocytes, Ly6C^{lo} monocytes and neutrophils) and adaptive (CD4^{+} T cells, CD8^{+} T cells and B cells) in the bone marrow **(D)**, spleen **(E)** and inguinal lymph nodes **(F)** of 8–12-week-old *Mlkl*$^{WT/WT}$, *Mlkl*$^{WT/S131P}$, and *Mlkl*$^{S131P/S131P}$ mice. Each symbol represents one individual mouse sampled and error bars represent mean ± SEM for *n=7-11* mice as indicated. **(G, H)** Immortalized mouse dermal fibroblasts (MDFs) were isolated from *Mlkl*$^{WT/WT}$, *Mlkl*$^{WT/S131P}$, and *Mlkl*$^{S131P/S131P}$ mice and stimulated as indicated for 6 hours for western blot analysis **(G)** or 24 hours for quantification of PI-positive cells using IncuCyte S3 live cell imaging **(H)**. Death data represent

mean ± SEM for independently generated cell lines of *n*=3-5. *p<0.05, **p<0.01 calculated using an unpaired, two-tailed Students t-test.

Figure 3. *Mlkl*^{S131P} mice show delayed recovery from myelosuppressive irradiation.

Peripheral red blood cells **(A)**, platelets **(B)** and monocytes **(C)** in *Mlkl*$^{WT/WT}$, *Mlkl*$^{WT/S131P}$, and *Mlkl*$^{S131P/S131P}$ mice following treatment with 5.5 Gy radiation. Quantified nucleated viable cells **(D)**, progenitor **(E)** and LSK **(F)** populations in the bone marrow of mice after myelosuppressive radiation. Mean ± SEM of *n*=3-10 independent mice from two separate experiments. Bone marrow from *Mlkl*$^{WT/WT}$ or *Mlkl*$^{S131P/S131P}$ mice on CD45$^{Ly5.2}$ background was mixed with wild-type GFP^{+} competitor bone marrow on a CD45$^{Ly5.2}$ background and transplanted into irradiated CD45$^{Ly5.1}$ recipients. Relative donor contribution to PBMCs **(G)**, red blood cells **(H)** and platelets **(I)** was assessed at 6 weeks post-transplantation. Mean shown of 2 donors per genotype, and 2-3 recipients per donor. Host contribution (CD45$^{Ly5.1}$) depicted in pink, GFP competitor in green and test (*Mlkl*$^{WT/WT}$ or *Mlkl*$^{S131P/S131P}$) in purple. *p<0.05, **p<0.01, ***p<0.001 calculated using an unpaired, two-tailed Students t-test **(A-F)**.

Figure 4. *Mlkl*^{S131P} recruited inflammatory neutrophils are less sensitive to TNF-induced necroptosis.

(A-D) Flow cytometry quantification of peritoneal innate (macrophages, Ly6C^{hi} monocytes, Ly6C^{lo} monocytes and neutrophils) and adaptive (CD4^{+} T cells, CD8^{+} T cells and B cells) immune cells at 4- **(A, B)** or 24- **(C, D)** hours post zymosan injection. ADVIA hematology quantification of circulating immune cells (lymphocytes, neutrophils and monocytes) at 4- **(E)** and 24- **(F)** hours post zymosan injection. Each symbol represents one independent animal, with mice from the 4- or 24-hour timepoint pooled from 3 and 2 independent zymosan experiments respectively. Error bars

represent mean ± SEM for *n=5-14* mice as indicated **(A-H)**. Evaluation of spontaneous apoptotic **(G)** or induced necroptotic signaling **(H)** in neutrophils recruited and isolated from the peritoneum 4 hours post-zymosan injection. Neutrophils were left unstimulated (spontaneous apoptosis) or treated with necroptotic stimulus (TNF, SMAC mimetic, IDN-6556; TSI) for 16 hours and cell death was measured every hour by percentage of SYTOX Green positive cells quantified using IncuCyte SX5 live cell imaging. Data were collected from one independent experiment with male and female data pooled, neutrophils isolated from independent mice with mean ± SEM of *n*=6-14 presented. ***p<0.001 calculated using an unpaired, two-tailed Students t-test.

Figure 5. *Mlkl*^{S131P} homozygote mice exhibit bacterial clearance defects following oral *Salmonella* infection.

(A) ZO-1 (yellow) and CD68 (purple) staining in epithelial barrier of intestinal sections taken at 14-days post *Salmonella* infection. **(B)** Increased bacterial burden observed in spleen and liver, but not feces in *Mlkl*$^{S131P/S131P}$ mice at infection endpoint. Quantification of circulating white blood cells (lymphocytes, neutrophils and monocytes) using ADVIA hematology **(C)** and splenic adaptive (CD4^{+} T cells, CD8^{+} T cells and B cells) and innate (macrophages, Ly6C^{hi} monocytes, Ly6C^{lo} monocytes and neutrophils) immune cells using flow cytometry **(D, E)**. *Salmonella* infection was performed on 3 independent occasions, with each symbol representing an individual mouse sampled. Error bars represent mean ± SEM for *n=9-16* mice as indicated. *p<0.05, **p<0.01, ***p<0.001 calculated using a Mann-Whitney test **(B)** or an unpaired, two-tailed Students t-test **(C-E)**.

Supplementary Figure 1. MLKL^{S132P} is less sensitive to inhibition by necrosulfonamide.

(**A)** Peripheral blood mononuclear cells (PBMCs) isolated from patient 2 and an aged matched healthy donor control were stimulated as indicated for 4 hours for western blot analysis. (**B)** ELISA measurement of supernatant TNF in PBMCs stimulated with LPS or Poly I:C for 5 hours. Mean of technical triplicates presented. **(C-F)** Evaluation of necroptotic signaling by $MLKL^{WT}$, $MLKL^{S132P}$ and $MLKL^{TSEE}$ in *MLKL*$^{-/-}$ **(C)** or WT **(D)** HT29 cells and WT **(E)** or *MLKL*$^{-/-}$ **(F)** U937 cells. Human MLKL expression was induced with doxycycline (Dox) and treated with necroptotic stimulus (TNF, SMAC mimetic, IDN-6556; TSI) in the presence or absence of MLKL inhibitor necrosulfonamide (NSA). Cell death was measured every hour for 24 hours by percentage of SYTOX Green positive cells quantified using IncuCyte SX5 or S3 live cell imaging. Independent cell lines were assayed in *n=2-9* experiments, with errors bars indicating the mean ± SEM. **(G, H)** Western blot analyses of whole cell lysates of doxycycline induced WT or *MLKL*$^{-/-}$ HT29 **(G)** or U937 **(H)** cells expressing $MLKL^{WT}$, $MLKL^{S132P}$ or $MLKL^{TSEE}$. **(I)** Blue-Native PAGE crude cytoplasm fractions of *MLKL*$^{-/-}$ HT29 cells under TSI stimulation (0-6 hours) in the presence or absence of NSA. **(J)** Western blot analyses of whole cell lysates taken 5 h post TSI stimulation in the presence or absence of NSA from doxycycline induced *MLKL*$^{-/-}$ HT29 cells expressing $MLKL^{WT}$, $MLKL^{S132P}$, $MLKL^{S83D}$ or $MLKL^{S83D,S132P}$. **(K, L)** Evaluation of necroptotic signaling in *MLKL*$^{-/-}$ **(K)** or WT **(L)** HT29 cells expressing $MLKL^{WT}$, $MLKL^{S132P}$, $MLKL^{S83D}$ and $MLKL^{S83D,S132P}$. Human MLKL expression was induced with doxycycline (Dox) and cells treated with necroptotic stimulus (TNF, SMAC mimetic, IDN-6556; TSI) in the presence or absence of MLKL inhibitor necrosulfonamide (NSA). Cell death was measured every hour for 23 hours by percentage of SYTOX-green positive cells quantified using IncuCyte SX5 or S3 live cell imaging. Independent cell lines were assayed in *n=4* experiments, with errors bars indicating the mean ±

SEM. Blots images in **A, G, H, I & J** are representative images of at least two independent repeat experiments.

Supplementary Figure 2. Cells expressing endogenous MLKL^{S131P} exhibit reduced TSI-induced necroptotic cell death.

(A) Representative images of H&E staining of salivary glands, mediastinum, liver and lung from 7–9-month-old *Mlkl*$^{WT/WT}$ and *Mlkl*$^{S131P/S131P}$ mice. Images are representative of *n=2* mice per genotype. **(B-D)** ADVIA hematology quantification of circulating red blood cells **(B)**, platelets **(C)** and white blood cells **(D)** in *Mlkl*$^{WT/WT}$, *Mlkl*$^{WT/S131P}$ and *Mlkl*$^{S131P/S131P}$ mice across age. Each symbol represents one independent mouse sampled and error bars represent mean ± SEM for *n=12-38* mice as indicated. (**E-V)** Flow cytometry quantification of innate (Ly6C^{hi}, Ly6C^{lo} and neutrophils) and adaptative (B cells, CD4^{+} T cells and CD8^{+} T cells) immune cells in the bone marrow **(E-J)**, spleen **(K-P)** and inguinal lymph nodes **(Q-V)** of 8–12-week-old basal state *Mlkl*$^{WT/WT}$, *Mlkl*$^{WT/S131P}$, and *Mlkl*$^{S131P/S131P}$ mice as indicated. Each symbol represents one independent mouse sampled and error bars represent mean ± SEM for *n=7-11* mice as indicated. **(W, X)** Primary mouse dermal fibroblasts (MDFs) were isolated from *Mlkl*$^{WT/WT}$, *Mlkl*$^{WT/S131P}$, and *Mlkl*$^{S131P/S131P}$ mice and stimulated as indicated for 6 hours for western blot analysis **(W)** or 20 hours for quantification of PI-positive cells using IncuCyte S3 live cell imaging **(X)**. **(Y, Z)** Bone marrow derived macrophages were isolated from *Mlkl*$^{WT/WT}$, *Mlkl*$^{WT/S131P}$, and *Mlkl*$^{S131P/S131P}$ mice and stimulated on day 6 of culture as indicated for 6 hours for western blot analysis **(Y)** or 24 hours for quantification of PI-positive cells using IncuCyte S3 live cell imaging **(Z)**. *$p<0.05$ **$p<0.01$ calculated using an unpaired, two-tailed Students t-test.

Supplementary Figure 3. *Mlkl*$^{S131P/S131P}$ hematopoietic stem cells transplanted in excess are outcompeted at 6-weeks post-transplant.

Bone marrow from *Mlkl*$^{S131P/S131P}$ mice on CD45$^{Ly5.2}$ background was mixed with wild-type GFP^{+} competitor bone marrow on a CD45$^{Ly5.2}$ background at a 70:30 ratio and transplanted into irradiated CD45$^{Ly5.1}$ recipients. Relative donor contribution to PBMCs **(A)**, red blood cells **(B)** and platelets **(C)** was assessed at 6 weeks post-transplantation. Mean ± SEM shown of 2 donors per genotype, and 3 recipients per donor. Host contribution (CD45$^{Ly5.1}$) depicted in pink, GFP competitor in green and test *Mlkl*$^{S131P/S131P}$ in purple.

Supplementary Figure 4. *Mlkl*^{S131P} mice have reduced levels of Ly6C^{hi} monocytes in the peritoneal lavage at 24-hours post zymosan injection.

(A-P) Flow cytometry quantification of peritoneal innate (macrophages, Ly6C^{hi}, Ly6C^{lo} and neutrophils) and adaptive (CD4^{+} T cells, CD8^{+} T cells and B cells) immune cells at 4- **(A-H)** or 24- **(I-P)** hours post-intraperitoneal injection of zymosan as indicated. **(Q-V)** ADVIA hematology quantification of peripheral blood cells (lymphocytes, neutrophils, and monocytes) at 4- **(Q-S)** and 24- **(T-V)** post-injection of zymosan. Each symbol represents one independent animal, with mice from the 4- or 24-hour timepoint pooled from 3 and 2 independent zymosan experiments respectively. Error bars represent mean ± SEM for *n=2-10* mice as indicated. *p<0.05 **p<0.01 calculated using an unpaired, two-tailed Students t-test.

Supplementary Figure 5. *Mlkl*^{S131P} does not abrogate death of BMDMs upon *in vitro Salmonella* infection.

(A, B) *Mlkl*$^{WT/WT}$, *Mlkl*$^{WT/S131P}$, and *Mlkl*$^{S131P/S131P}$ mice were infected with *Salmonella* via oral gavage and monitored for 14-days by daily body weight **(A)** and temperature **(B)** measurements. (**C-E)** Bacterial burden calculation of *Salmonella* colonization in the spleen **(C)**, liver **(D)**, and feces **(E)** at experimental endpoint. **(F-H)** ADVIA hematology quantification of peripheral monocytes **(F)**, lymphocytes **(G)** and neutrophils **(H). (I-O)** Splenic adaptive (CD4^{+} T cells, CD8^{+} T cells and B cells) **(I-K)** and innate (macrophages, Ly6C^{hi}, Ly6C^{lo} and neutrophils) **(L-O)** immune cells were quantified by flow cytometry at experimental endpoint. *Salmonella* infection was completed 3 independent times, with each symbol representing an individual mouse sampled. Error bars represent mean ± SEM for *n=3-9* mice as indicated. **(P, Q)** *In vitro* assessment of *Salmonella* SL1344 infection of primary BMDMs generated from *Mlkl*$^{WT/WT}$, *Mlkl*$^{WT/S131P}$, and *Mlkl*$^{S131P/S131P}$ mice. **(G)** BMDMs were infected with *Salmonella* (MOI:25) and cleavage associated with Gasdermin-D activation during pyroptosis was analyzed by immunoblotting at the indicated time points. **(H)** LDH release cell death assay of BMDMs after infection with *Salmonella* (MOI:10 or MOI:50) at indicated time points. *In vitro Salmonella* experiment completed once, with mean ± SEM for *n=3* individual mice shown. Blot images in **(G)** are representative of independent duplicates.

ACKNOWLEDGEMENTS

We thank all the following people for their technical assistance; Aira Nuguid and Tina Cardamone (Phenomics Australia Histopathology and Slide Scanning Service- The University of Melbourne). WEHI Cytometry Facility, WEHI Antibody Facility, WEHI Centre for Dynamic Imaging, WEHI Bioservices, Cheree Fitzgibbon (WEHI), Jacinta Hansen (WEHI) and Matthew Cook (ANU). The generation of *Mlkl*^{S131P} mice by CRISPR/Cas9 gene editing was performed by Andrew Kueh and

Marco Herold (WEHI MAGEC laboratory) supported by the Australian Phenomics Network (APN) and the Australian Government through the National Collaborative Research Infrastructure Strategy (NCRIS) program. We thank Warren Alexander, Melanie Bahlo and Ian Wicks for the provision of important resources and expertise. We are grateful to the National Health and Medical Research Council for fellowship (J.M.H., 1142669; A.L.S., 2002965; J.M.M., 1172929; J.S., 1107149), grant (J.M.M., 1105023; K.R.M., 1092602; J.S., 1105023; J.M.H., 2011584) and infrastructure (IRIISS 9000719); Arthritis Australia support to K.R.M. We acknowledge scholarship support for S.E.G and D.F (Australian Government Research Training Program Stipend Scholarships), S.E.G (Wendy Dowsett Scholarship), S.C (Walter and Eliza Hall Handman PhD Scholarship). Victorian State Government Operational Infrastructure Support Scheme.

AUTHOR INFORMATION

The Walter and Eliza Hall Institute of Medical Research, Parkville, VIC, 3052, Australia

Sarah E. Garnish, Katherine R. Martin, Maria Kauppi, Victoria Jackson, Daniel Frank, Emma C. Tovey Crutchfield, Komal M. Patel, Shene Chiou, Andre L. Samson, Marcel Doerflinger, Christopher R. Horne, Cathrine Hall, Samuel N. Young, Charlotte Slade, John Silke, James M. Murphy and Joanne M. Hildebrand

Department of Medical Biology, University of Melbourne, Parkville, VIC, 3052, Australia

Sarah E. Garnish, Katherine R. Martin, Maria Kauppi, Victoria Jackson, Daniel Frank, Shene Chiou, Andre L. Samson, Charlotte Slade, John Silke, James M. Murphy and Joanne M. Hildebrand

Centre for Innate Immunity and Infectious Diseases, Hudson Institute of Medical Research, Clayton, VIC, 3168, Australia

Rebecca Ambrose, Vik Ven Eng and Jaclyn S. Pearson

Department of Molecular and Translational Science, Monash University, Clayton, VIC, 3168, Australia

Rebecca Ambrose, Vik Ven Eng and Jaclyn S. Pearson

Department of Microbiology, Monash University, Clayton, VIC, 3168, Australia

Jaclyn S. Pearson

Department of Immunology and Infection, John Curtin School of Medical Research, Australian National University, ACT, Australia

Vicki Athanasopoulos and Carola Vinuesa

Department of Clinical Immunology and Allergy, Royal Melbourne Hospital, Parkville, VIC, 3052, Australia

Charlotte Slade

Institute of Virology, Technical University of Munich/Helmholtz Munich, Munich, Germany

Gregor Ebert

Contributions

Conceptualization: S.E.G., J.S., J.M.M., J.M.H. Methodology: S.E.G., K.R.M., M.K., V.J., R.A., V.E., D.F., S.C., A.L.S., M.D., C.R.H., C.H., S.N.Y., J.S.P., G.E., J.M.H. Resources: K.R.M., M.K., V.A., C.V., C.S., J.S.P., J.S., J.M.M., J.M.H. Supervision: K.M., M.K., J.S., J.M.M., J.M.H. Funding acquisition: J.S., J.M.M., J.M.H. S.E.G and J.M.H co-wrote the paper with input from authors.

ETHICS DECLARATIONS

Competing interests: S.E.G, K.M.P, A.L.S, C.R.H, S.N.Y, J.S, J.M.M and J.M.H contribute, or have contributed, to a project developing necroptosis inhibitors in collaboration with Anaxis Pty Ltd. K.R.M received funding from CSL Pty Ltd. The remaining authors declare no competing interests.

References

Boisson-Dupuis, S., N. Ramirez-Alejo, Z. Li, E. Patin, G. Rao, G. Kerner, C.K. Lim, D.N. Krementsov, N. Hernandez, C.S. Ma, Q. Zhang, J. Markle, R. Martinez-Barricarte, K. Payne, R. Fisch, C. Deswarte, J. Halpern, M. Bouaziz, J. Mulwa, D. Sivanesan, T. Lazarov, R. Naves, P. Garcia, Y. Itan, B. Boisson,

857 A. Checchi, F. Jabot-Hanin, A. Cobat, A. Guennoun, C.C. Jackson, S. Pekcan, Z. Caliskaner, J.
858 Inostroza, B.T. Costa-Carvalho, J.A.T. de Albuquerque, H. Garcia-Ortiz, L. Orozco, T. Ozcelik, A.
859 Abid, I.A. Rhorfi, H. Souhi, H.N. Amrani, A. Zegmout, F. Geissmann, S.W. Michnick, I. Muller-
860 Fleckenstein, B. Fleckenstein, A. Puel, M.J. Ciancanelli, N. Marr, H. Abolhassani, M.E. Balcells, A.
861 Condino-Neto, A. Strickler, K. Abarca, C. Teuscher, H.D. Ochs, I. Reisli, E.H. Sayar, J. El-Baghdadi, J.
862 Bustamante, L. Hammarstrom, S.G. Tangye, S. Pellegrini, L. Quintana-Murci, L. Abel, and J.L.
863 Casanova. 2018. Tuberculosis and impaired IL-23-dependent IFN-gamma immunity in humans
864 homozygous for a common TYK2 missense variant. *Sci Immunol* 3:
865 Boomer, J.S., K. To, K.C. Chang, O. Takasu, D.F. Osborne, A.H. Walton, T.L. Bricker, S.D. Jarman, 2nd, D.
866 Kreisel, A.S. Krupnick, A. Srivastava, P.E. Swanson, J.M. Green, and R.S. Hotchkiss. 2011.
867 Immunosuppression in patients who die of sepsis and multiple organ failure. *JAMA* 306:2594-
868 2605.
869 Bossen, C., K. Ingold, A. Tardivel, J.L. Bodmer, O. Gaide, S. Hertig, C. Ambrose, J. Tschopp, and P. Schneider.
870 2006. Interactions of tumor necrosis factor (TNF) and TNF receptor family members in the mouse
871 and human. *J Biol Chem* 281:13964-13971.
872 Brinkworth, J.F., and N. Valizadegan. 2021. Sepsis and the evolution of human increased sensitivity to
873 lipopolysaccharide. *Evol Anthropol* 30:141-157.
874 Cai, Z., S. Jitkaew, J. Zhao, H.C. Chiang, S. Choksi, J. Liu, Y. Ward, L.G. Wu, and Z.G. Liu. 2014. Plasma
875 membrane translocation of trimerized MLKL protein is required for TNF-induced necroptosis. *Nat*
876 *Cell Biol* 16:55-65.
877 Chen, X., W. Li, J. Ren, D. Huang, W.T. He, Y. Song, C. Yang, W. Li, X. Zheng, P. Chen, and J. Han. 2014.
878 Translocation of mixed lineage kinase domain-like protein to plasma membrane leads to necrotic
879 cell death. *Cell research* 24:105-121.
880 Cortes, A., J. Hadler, J.P. Pointon, P.C. Robinson, T. Karaderi, P. Leo, K. Cremin, K. Pryce, J. Harris, S. Lee,
881 K.B. Joo, S.C. Shim, M. Weisman, M. Ward, X. Zhou, H.J. Garchon, G. Chiocchia, J. Nossent, B.A.
882 Lie, O. Forre, J. Tuomilehto, K. Laiho, L. Jiang, Y. Liu, X. Wu, L.A. Bradbury, D. Elewaut, R. Burgos-
883 Vargas, S. Stebbings, L. Appleton, C. Farrah, J. Lau, T.J. Kenna, N. Haroon, M.A. Ferreira, J. Yang, J.
884 Mulero, J.L. Fernandez-Sueiro, M.A. Gonzalez-Gay, C. Lopez-Larrea, P. Deloukas, P. Donnelly, C.
885 Australo-Anglo-American Spondyloarthritis, S. Groupe Francaise d'Etude Genetique des, S. Nord-
886 Trondelag Health, C. Spondyloarthritis Research Consortium of, C. Wellcome Trust Case Control,
887 P. Bowness, K. Gafney, H. Gaston, D.D. Gladman, P. Rahman, W.P. Maksymowych, H. Xu, J.B.
888 Crusius, I.E. van der Horst-Bruinsma, C.T. Chou, R. Valle-Onate, C. Romero-Sanchez, I.M. Hansen,
889 F.M. Pimentel-Santos, R.D. Inman, V. Videm, J. Martin, M. Breban, J.D. Reveille, D.M. Evans, T.H.
890 Kim, B.P. Wordsworth, and M.A. Brown. 2013. Identification of multiple risk variants for
891 ankylosing spondylitis through high-density genotyping of immune-related loci. *Nat Genet*
892 45:730-738.
893 Cortes, A., S.L. Pulit, P.J. Leo, J.J. Pointon, P.C. Robinson, M.H. Weisman, M. Ward, L.S. Gensler, X. Zhou,
894 H.J. Garchon, G. Chiocchia, J. Nossent, B.A. Lie, O. Forre, J. Tuomilehto, K. Laiho, L.A. Bradbury, D.
895 Elewaut, R. Burgos-Vargas, S. Stebbings, L. Appleton, C. Farrah, J. Lau, N. Haroon, J. Mulero, F.J.
896 Blanco, M.A. Gonzalez-Gay, C. Lopez-Larrea, P. Bowness, K. Gaffney, H. Gaston, D.D. Gladman, P.
897 Rahman, W.P. Maksymowych, J.B. Crusius, I.E. van der Horst-Bruinsma, R. Valle-Onate, C.
898 Romero-Sanchez, I.M. Hansen, F.M. Pimentel-Santos, R.D. Inman, J. Martin, M. Breban, B.P.
899 Wordsworth, J.D. Reveille, D.M. Evans, P.I. de Bakker, and M.A. Brown. 2015. Major
900 histocompatibility complex associations of ankylosing spondylitis are complex and involve further
901 epistasis with ERAP1. *Nat Commun* 6:7146.
902 Dondelinger, Y., W. Declercq, S. Montessuit, R. Roelandt, A. Goncalves, I. Bruggeman, P. Hulpiau, K.
903 Weber, C.A. Sehon, R.W. Marquis, J. Bertin, P.J. Gough, S. Savvides, J.C. Martinou, M.J. Bertrand,

904 and P. Vandenabeele. 2014. MLKL compromises plasma membrane integrity by binding to
905 phosphatidylinositol phosphates. *Cell reports* 7:971-981.
906 Evans, D.M., C.C. Spencer, J.J. Pointon, Z. Su, D. Harvey, G. Kochan, U. Oppermann, A. Dilthey, M. Pirinen,
907 M.A. Stone, L. Appleton, L. Moutsianas, S. Leslie, T. Wordsworth, T.J. Kenna, T. Karaderi, G.P.
908 Thomas, M.M. Ward, M.H. Weisman, C. Farrar, L.A. Bradbury, P. Danoy, R.D. Inman, W.
909 Maksymowych, D. Gladman, P. Rahman, C. Spondyloarthritis Research Consortium of, A. Morgan,
910 H. Marzo-Ortega, P. Bowness, K. Gaffney, J.S. Gaston, M. Smith, J. Bruges-Armas, A.R. Couto, R.
911 Sorrentino, F. Paladini, M.A. Ferreira, H. Xu, Y. Liu, L. Jiang, C. Lopez-Larrea, R. Diaz-Pena, A. Lopez-
912 Vazquez, T. Zayats, G. Band, C. Bellenguez, H. Blackburn, J.M. Blackwell, E. Bramon, S.J.
913 Bumpstead, J.P. Casas, A. Corvin, N. Craddock, P. Deloukas, S. Dronov, A. Duncanson, S. Edkins, C.
914 Freeman, M. Gillman, E. Gray, R. Gwilliam, N. Hammond, S.E. Hunt, J. Jankowski, A. Jayakumar, C.
915 Langford, J. Liddle, H.S. Markus, C.G. Mathew, O.T. McCann, M.I. McCarthy, C.N. Palmer, L.
916 Peltonen, R. Plomin, S.C. Potter, A. Rautanen, R. Ravindrarajah, M. Ricketts, N. Samani, S.J.
917 Sawcer, A. Strange, R.C. Trembath, A.C. Viswanathan, M. Waller, P. Weston, P. Whittaker, S.
918 Widaa, N.W. Wood, G. McVean, J.D. Reveille, B.P. Wordsworth, M.A. Brown, P. Donnelly, C.
919 Australo-Anglo-American Spondyloarthritis, and C. Wellcome Trust Case Control. 2011.
920 Interaction between ERAP1 and HLA-B27 in ankylosing spondylitis implicates peptide handling in
921 the mechanism for HLA-B27 in disease susceptibility. *Nat Genet* 43:761-767.
922 Faergeman, S.L., H. Evans, K.E. Attfield, C. Desel, S.B. Kuttikkatte, M. Sommerlund, L.T. Jensen, J. Frokiaer,
923 M.A. Friese, P.M. Matthews, C. Luchtenborg, B. Brugger, A.B. Oturai, C.A. Dendrou, and L. Fugger.
924 2020. A novel neurodegenerative spectrum disorder in patients with MLKL deficiency. *Cell death*
925 *& disease* 11:303.
926 Galan, J.E. 2021. Salmonella Typhimurium and inflammation: a pathogen-centric affair. *Nat Rev Microbiol*
927 19:716-725.
928 Garnish, S.E., and J.M. Hildebrand. 2022. Rare catastrophes and evolutionary legacies: human germline
929 gene variants in MLKL and the necroptosis signalling pathway. *Biochem Soc Trans* 50:529-539.
930 Garnish, S.E., Y. Meng, A. Koide, J.J. Sandow, E. Denbaum, A.V. Jacobsen, W. Yeung, A.L. Samson, C.R.
931 Horne, C. Fitzgibbon, S.N. Young, P.P.C. Smith, A.I. Webb, E.J. Petrie, J.M. Hildebrand, N. Kannan,
932 P.E. Czabotar, S. Koide, and J.M. Murphy. 2021. Conformational interconversion of MLKL and
933 disengagement from RIPK3 precede cell death by necroptosis. *Nat Commun* 12:2211.
934 Gutierrez-Arcelus, M., S.S. Rich, and S. Raychaudhuri. 2016. Autoimmune diseases - connecting risk alleles
935 with molecular traits of the immune system. *Nat Rev Genet* 17:160-174.
936 He, S., Y. Liang, F. Shao, and X. Wang. 2011. Toll-like receptors activate programmed necrosis in
937 macrophages through a receptor-interacting kinase-3-mediated pathway. *Proc Natl Acad Sci U S*
938 *A* 108:20054-20059.
939 He, S., L. Wang, L. Miao, T. Wang, F. Du, L. Zhao, and X. Wang. 2009. Receptor interacting protein kinase-
940 3 determines cellular necrotic response to TNF-alpha. *Cell* 137:1100-1111.
941 Hildebrand, J.M., M. Kauppi, I.J. Majewski, Z. Liu, A.J. Cox, S. Miyake, E.J. Petrie, M.A. Silk, Z. Li, M.C. Tanzer,
942 G. Brumatti, S.N. Young, C. Hall, S.E. Garnish, J. Corbin, M.D. Stutz, L. Di Rago, P. Gangatirkar, E.C.
943 Josefsson, K. Rigbye, H. Anderton, J.A. Rickard, A. Tripaydonis, J. Sheridan, T.S. Scerri, V.E. Jackson,
944 P.E. Czabotar, J.G. Zhang, L. Varghese, C.C. Allison, M. Pellegrini, G.M. Tannahill, E.C. Hatchell, T.A.
945 Willson, D. Stockwell, C.A. de Graaf, J. Collinge, A. Hilton, N. Silke, S.K. Spall, D. Chau, V.
946 Athanasopoulos, D. Metcalf, R.M. Laxer, A.G. Bassuk, B.W. Darbro, M.A. Fiatarone Singh, N.
947 Vlahovich, D. Hughes, M. Kozlovskaia, D.B. Ascher, K. Warnatz, N. Venhoff, J. Thiel, C. Biben, S.
948 Blum, J. Reveille, M.S. Hildebrand, C.G. Vinuesa, P. McCombe, M.A. Brown, B.T. Kile, C. McLean,
949 M. Bahlo, S.L. Masters, H. Nakano, P.J. Ferguson, J.M. Murphy, W.S. Alexander, and J. Silke. 2020.
950 A missense mutation in the MLKL brace region promotes lethal neonatal inflammation and
951 hematopoietic dysfunction. *Nat Commun* 11:3150.

952 Hildebrand, J.M., B. Lo, S. Tomei, V. Mattei, S.N. Young, C. Fitzgibbon, J.M. Murphy, and A. Fadda. 2021. A
953 family harboring an MLKL loss of function variant implicates impaired necroptosis in diabetes. *Cell*
954 *death & disease* 12:345.
955 Hildebrand, J.M., M.C. Tanzer, I.S. Lucet, S.N. Young, S.K. Spall, P. Sharma, C. Pierotti, J.M. Garnier, R.C.
956 Dobson, A.I. Webb, A. Tripaydonis, J.J. Babon, M.D. Mulcair, M.J. Scanlon, W.S. Alexander, A.F.
957 Wilks, P.E. Czabotar, G. Lessene, J.M. Murphy, and J. Silke. 2014. Activation of the pseudokinase
958 MLKL unleashes the four-helix bundle domain to induce membrane localization and necroptotic
959 cell death. *Proceedings of the National Academy of Sciences of the United States of America*
960 111:15072-15077.
961 Hohmann, E.L. 2001. Nontyphoidal salmonellosis. *Clin Infect Dis* 32:263-269.
962 Holler, N., R. Zaru, O. Micheau, M. Thome, A. Attinger, S. Valitutti, J.L. Bodmer, P. Schneider, B. Seed, and
963 J. Tschopp. 2000. Fas triggers an alternative, caspase-8-independent cell death pathway using the
964 kinase RIP as effector molecule. *Nat Immunol* 1:489-495.
965 Huang, Z., A.H. Rose, F.W. Hoffmann, A.S. Hashimoto, P. Bertino, T. Denk, J. Takano, N. Iwata, T.C. Saido,
966 and P.R. Hoffmann. 2013. Calpastatin prevents NF-kappaB-mediated hyperactivation of
967 macrophages and attenuates colitis. *J Immunol* 191:3778-3788.
968 Kaiser, W.J., H. Sridharan, C. Huang, P. Mandal, J.W. Upton, P.J. Gough, C.A. Sehon, R.W. Marquis, J. Bertin,
969 and E.S. Mocarski. 2013. Toll-like receptor 3-mediated necrosis via TRIF, RIP3, and MLKL. *J Biol*
970 *Chem* 288:31268-31279.
971 Karczewski, K.J., L.C. Francioli, G. Tiao, B.B. Cummings, J. Alfoldi, Q. Wang, R.L. Collins, K.M. Laricchia, A.
972 Ganna, D.P. Birnbaum, L.D. Gauthier, H. Brand, M. Solomonson, N.A. Watts, D. Rhodes, M. Singer-
973 Berk, E.M. England, E.G. Seaby, J.A. Kosmicki, R.K. Walters, K. Tashman, Y. Farjoun, E. Banks, T.
974 Poterba, A. Wang, C. Seed, N. Whiffin, J.X. Chong, K.E. Samocha, E. Pierce-Hoffman, Z. Zappala,
975 A.H. O'Donnell-Luria, E.V. Minikel, B. Weisburd, M. Lek, J.S. Ware, C. Vittal, I.M. Armean, L.
976 Bergelson, K. Cibulskis, K.M. Connolly, M. Covarrubias, S. Donnelly, S. Ferriera, S. Gabriel, J.
977 Gentry, N. Gupta, T. Jeandet, D. Kaplan, C. Llanwarne, R. Munshi, S. Novod, N. Petrillo, D. Roazen,
978 V. Ruano-Rubio, A. Saltzman, M. Schleicher, J. Soto, K. Tibbetts, C. Tolonen, G. Wade, M.E.
979 Talkowski, C. Genome Aggregation Database, B.M. Neale, M.J. Daly, and D.G. MacArthur. 2020.
980 The mutational constraint spectrum quantified from variation in 141,456 humans. *Nature*
981 581:434-443.
982 Karunakaran, D., A.W. Turner, A.C. Duchez, S. Soubeyrand, A. Rasheed, D. Smyth, D.P. Cook, M. Nikpay,
983 J.W. Kandiah, C. Pan, M. Geoffrion, R. Lee, L. Boytard, H. Wyatt, M.A. Nguyen, P. Lau, M. Laakso,
984 B. Ramkhelawon, M. Alvarez, K.H. Pietilainen, P. Pajukanta, B.C. Vanderhyden, P. Liu, S.B. Berger,
985 P.J. Gough, J. Bertin, M.E. Harper, A.J. Lusis, R. McPherson, and K.J. Rayner. 2020. RIPK1 gene
986 variants associate with obesity in humans and can be therapeutically silenced to reduce obesity
987 in mice. *Nat Metab* 2:1113-1125.
988 Kerner, G., G. Laval, E. Patin, S. Boisson-Dupuis, L. Abel, J.L. Casanova, and L. Quintana-Murci. 2021.
989 Human ancient DNA analyses reveal the high burden of tuberculosis in Europeans over the last
990 2,000 years. *Am J Hum Genet* 108:517-524.
991 Key, F.M., C. Posth, L.R. Esquivel-Gomez, R. Hubler, M.A. Spyrou, G.U. Neumann, A. Furtwangler, S. Sabin,
992 M. Burri, A. Wissgott, A.K. Lankapalli, A.J. Vagene, M. Meyer, S. Nagel, R. Tukhbatova, A. Khokhlov,
993 A. Chizhevsky, S. Hansen, A.B. Belinsky, A. Kalmykov, A.R. Kantorovich, V.E. Maslov, P.W.
994 Stockhammer, S. Vai, M. Zavattaro, A. Riga, D. Caramelli, R. Skeates, J. Beckett, M.G. Gradoli, N.
995 Steuri, A. Hafner, M. Ramstein, I. Siebke, S. Losch, Y.S. Erdal, N.F. Alikhan, Z. Zhou, M. Achtman,
996 K. Bos, S. Reinhold, W. Haak, D. Kuhnert, A. Herbig, and J. Krause. 2020. Emergence of human-
997 adapted Salmonella enterica is linked to the Neolithization process. *Nat Ecol Evol* 4:324-333.
998 Kirino, Y., G. Bertsias, Y. Ishigatsubo, N. Mizuki, I. Tugal-Tutkun, E. Seyahi, Y. Ozyazgan, F.S. Sacli, B. Erer,
999 H. Inoko, Z. Emrence, A. Cakar, N. Abaci, D. Ustek, C. Satorius, A. Ueda, M. Takeno, Y. Kim, G.M.

1000 Wood, M.J. Ombrello, A. Meguro, A. Gul, E.F. Remmers, and D.L. Kastner. 2013. Genome-wide
1001 association analysis identifies new susceptibility loci for Behcet's disease and epistasis between
1002 HLA-B*51 and ERAP1. *Nat Genet* 45:202-207.
1003 Kitur, K., S. Wachtel, A. Brown, M. Wickersham, F. Paulino, H.F. Penaloza, G. Soong, S. Bueno, D. Parker,
1004 and A. Prince. 2016. Necroptosis Promotes Staphylococcus aureus Clearance by Inhibiting
1005 Excessive Inflammatory Signaling. *Cell reports* 16:2219-2230.
1006 Li, J., T. McQuade, A.B. Siemer, J. Napetschnig, K. Moriwaki, Y.S. Hsiao, E. Damko, D. Moquin, T. Walz, A.
1007 McDermott, F.K. Chan, and H. Wu. 2012. The RIP1/RIP3 necrosome forms a functional amyloid
1008 signaling complex required for programmed necrosis. *Cell* 150:339-350.
1009 Liu, Z., L.F. Dagley, K. Shield-Artin, S.N. Young, A. Bankovacki, X. Wang, M. Tang, J. Howitt, C.A. Stafford,
1010 U. Nachbur, C. Fitzgibbon, S.E. Garnish, A.I. Webb, D. Komander, J.M. Murphy, J.M. Hildebrand,
1011 and J. Silke. 2021a. Oligomerization-driven MLKL ubiquitylation antagonizes necroptosis. *EMBO J*
1012 40:e103718.
1013 Liu, Z., H. Nailwal, J. Rector, M.M. Rahman, R. Sam, G. McFadden, and F.K. Chan. 2021b. A class of viral
1014 inducer of degradation of the necroptosis adaptor RIPK3 regulates virus-induced inflammation.
1015 *Immunity* 54:247-258 e247.
1016 Martin, K.R., M. Pederzoli-Ribeil, E. Pacreau, S.S. Burgener, A. Dahdah, C. Candalh, E. Lauret, M. Foretz, L.
1017 Mouthon, B. Lucas, N. Thieblemont, C. Benarafa, P. Launay, and V. Witko-Sarsat. 2017. Transgenic
1018 Mice Expressing Human Proteinase 3 Exhibit Sustained Neutrophil-Associated Peritonitis. *Journal*
1019 *of immunology* 199:3914-3924.
1020 Meng, Y., K.A. Davies, C. Fitzgibbon, S.N. Young, S.E. Garnish, C.R. Horne, C. Luo, J.M. Garnier, L.Y. Liang,
1021 A.D. Cowan, A.L. Samson, G. Lessene, J.J. Sandow, P.E. Czabotar, and J.M. Murphy. 2021. Human
1022 RIPK3 maintains MLKL in an inactive conformation prior to cell death by necroptosis. *Nat Commun*
1023 12:6783.
1024 Mompean, M., W. Li, J. Li, S. Laage, A.B. Siemer, G. Bozkurt, H. Wu, and A.E. McDermott. 2018. The
1025 Structure of the Necrosome RIPK1-RIPK3 Core, a Human Hetero-Amyloid Signaling Complex. *Cell*
1026 173:1244-1253 e1210.
1027 Murphy, J.M., P.E. Czabotar, J.M. Hildebrand, I.S. Lucet, J.G. Zhang, S. Alvarez-Diaz, R. Lewis, N. Lalaoui, D.
1028 Metcalf, A.I. Webb, S.N. Young, L.N. Varghese, G.M. Tannahill, E.C. Hatchell, I.J. Majewski, T.
1029 Okamoto, R.C.J. Dobson, D.J. Hilton, J.J. Babon, N.A. Nicola, A. Strasser, J. Silke, and W.S.
1030 Alexander. 2013. The Pseudokinase MLKL Mediates Necroptosis via a Molecular Switch
1031 Mechanism. *Immunity* 39:443-453.
1032 Murphy, J.M., I.S. Lucet, J.M. Hildebrand, M.C. Tanzer, S.N. Young, P. Sharma, G. Lessene, W.S. Alexander,
1033 J.J. Babon, J. Silke, and P.E. Czabotar. 2014. Insights into the evolution of divergent nucleotide-
1034 binding mechanisms among pseudokinases revealed by crystal structures of human and mouse
1035 MLKL. *The Biochemical journal* 457:369-377.
1036 Pearson, J.S., C. Giogha, S. Muhlen, U. Nachbur, C.L. Pham, Y. Zhang, J.M. Hildebrand, C.V. Oates, T.W.
1037 Lung, D. Ingle, L.F. Dagley, A. Bankovacki, E.J. Petrie, G.N. Schroeder, V.F. Crepin, G. Frankel, S.L.
1038 Masters, J. Vince, J.M. Murphy, M. Sunde, A.I. Webb, J. Silke, and E.L. Hartland. 2017. EspL is a
1039 bacterial cysteine protease effector that cleaves RHIM proteins to block necroptosis and
1040 inflammation. *Nat Microbiol* 2:16258.
1041 Petrie, E.J., R.W. Birkinshaw, A. Koide, E. Denbaum, J.M. Hildebrand, S.E. Garnish, K.A. Davies, J.J. Sandow,
1042 A.L. Samson, X. Gavin, C. Fitzgibbon, S.N. Young, P.J. Hennessy, P.P.C. Smith, A.I. Webb, P.E.
1043 Czabotar, S. Koide, and J.M. Murphy. 2020. Identification of MLKL membrane translocation as a
1044 checkpoint in necroptotic cell death using Monobodies. *Proceedings of the National Academy of*
1045 *Sciences of the United States of America* 117:8468-8475.
1046 Petrie, E.J., J.J. Sandow, A.V. Jacobsen, B.J. Smith, M.D.W. Griffin, I.S. Lucet, W. Dai, S.N. Young, M.C.
1047 Tanzer, A. Wardak, L.Y. Liang, A.D. Cowan, J.M. Hildebrand, W.J.A. Kersten, G. Lessene, J. Silke,

1048 P.E. Czabotar, A.I. Webb, and J.M. Murphy. 2018. Conformational switching of the pseudokinase
1049 domain promotes human MLKL tetramerization and cell death by necroptosis. *Nat Commun*
1050 9:2422.
1051 Petrie, E.J., J.J. Sandow, W.I.L. Lehmann, L.Y. Liang, D. Coursier, S.N. Young, W.J.A. Kersten, C. Fitzgibbon,
1052 A.L. Samson, A.V. Jacobsen, K.N. Lowes, A.E. Au, H. Jousset Sabroux, N. Lalaoui, A.I. Webb, G.
1053 Lessene, G. Manning, I.S. Lucet, and J.M. Murphy. 2019. Viral MLKL Homologs Subvert Necroptotic
1054 Cell Death by Sequestering Cellular RIPK3. *Cell Rep* 28:3309-3319 e3305.
1055 Pierdomenico, M., A. Negroni, L. Stronati, R. Vitali, E. Prete, J. Bertin, P.J. Gough, M. Aloi, and S. Cucchiara.
1056 2014. Necroptosis is active in children with inflammatory bowel disease and contributes to
1057 heighten intestinal inflammation. *Am J Gastroenterol* 109:279-287.
1058 Ramos, P.S., A.M. Shedlock, and C.D. Langefeld. 2015. Genetics of autoimmune diseases: insights from
1059 population genetics. *J Hum Genet* 60:657-664.
1060 Rickard, J.A., H. Anderton, N. Etemadi, U. Nachbur, M. Darding, N. Peltzer, N. Lalaoui, K.E. Lawlor, H.
1061 Vanyai, C. Hall, A. Bankovacki, L. Gangoda, W.W. Wong, J. Corbin, C. Huang, E.S. Mocarski, J.M.
1062 Murphy, W.S. Alexander, A.K. Voss, D.L. Vaux, W.J. Kaiser, H. Walczak, and J. Silke. 2014a. TNFR1-
1063 dependent cell death drives inflammation in Sharpin-deficient mice. *Elife* 3:
1064 Rickard, J.A., J.A. O'Donnell, J.M. Evans, N. Lalaoui, A.R. Poh, T. Rogers, J.E. Vince, K.E. Lawlor, R.L. Ninnis,
1065 H. Anderton, C. Hall, S.K. Spall, T.J. Phesse, H.E. Abud, L.H. Cengia, J. Corbin, S. Mifsud, L. Di Rago,
1066 D. Metcalf, M. Ernst, G. Dewson, A.W. Roberts, W.S. Alexander, J.M. Murphy, P.G. Ekert, S.L.
1067 Masters, D.L. Vaux, B.A. Croker, M. Gerlic, and J. Silke. 2014b. RIPK1 regulates RIPK3-MLKL-driven
1068 systemic inflammation and emergency hematopoiesis. *Cell* 157:1175-1188.
1069 Robinson, P.C., M.E. Costello, P. Leo, L.A. Bradbury, K. Hollis, A. Cortes, S. Lee, K.B. Joo, S.C. Shim, M.
1070 Weisman, M. Ward, X. Zhou, H.J. Garchon, G. Chiocchia, J. Nossent, B.A. Lie, O. Forre, J.
1071 Tuomilehto, K. Laiho, L. Jiang, Y. Liu, X. Wu, D. Elewaut, R. Burgos-Vargas, L.S. Gensler, S.
1072 Stebbings, N. Haroon, J. Mulero, J.L. Fernandez-Sueiro, M.A. Gonzalez-Gay, C. Lopez-Larrea, P.
1073 Bowness, K. Gafney, J.S. Gaston, D.D. Gladman, P. Rahman, W.P. Maksymowych, H. Xu, I.E. van
1074 der Horst-Bruinsma, C.T. Chou, R. Valle-Onate, M.C. Romero-Sanchez, I.M. Hansen, F.M. Pimentel-
1075 Santos, R.D. Inman, J. Martin, M. Breban, D. Evans, J.D. Reveille, T.H. Kim, B.P. Wordsworth, and
1076 M.A. Brown. 2015. ERAP2 is associated with ankylosing spondylitis in HLA-B27-positive and HLA-
1077 B27-negative patients. *Ann Rheum Dis* 74:1627-1629.
1078 Rodriguez, D.A., R. Weinlich, S. Brown, C. Guy, P. Fitzgerald, C.P. Dillon, A. Oberst, G. Quarato, J. Low, J.G.
1079 Cripps, T. Chen, and D.R. Green. 2016. Characterization of RIPK3-mediated phosphorylation of the
1080 activation loop of MLKL during necroptosis. *Cell Death Differ* 23:76-88.
1081 Samson, A.L., S.E. Garnish, J.M. Hildebrand, and J.M. Murphy. 2021. Location, location, location: A
1082 compartmentalized view of TNF-induced necroptotic signaling. *Science signaling* 14:
1083 Samson, A.L., Y. Zhang, N.D. Geoghegan, X.J. Gavin, K.A. Davies, M.J. Mlodzianoski, L.W. Whitehead, D.
1084 Frank, S.E. Garnish, C. Fitzgibbon, A. Hempel, S.N. Young, A.V. Jacobsen, W. Cawthorne, E.J. Petrie,
1085 M.C. Faux, K. Shield-Artin, N. Lalaoui, J.M. Hildebrand, J. Silke, K.L. Rogers, G. Lessene, E.D.
1086 Hawkins, and J.M. Murphy. 2020. MLKL trafficking and accumulation at the plasma membrane
1087 control the kinetics and threshold for necroptosis. *Nat Commun* 11:3151.
1088 Sethi, A., C.R. Horne, C. Fitzgibbon, K. Wilde, K.A. Davies, S.E. Garnish, A.V. Jacobsen, A.L. Samson, J.M.
1089 Hildebrand, A. Wardak, P.E. Czabotar, E.J. Petrie, P.R. Gooley, and J.M. Murphy. 2022. Membrane
1090 permeabilization is mediated by distinct epitopes in mouse and human orthologs of the
1091 necroptosis effector, MLKL. *Cell Death Differ*
1092 Strange, A., F. Capon, C.C. Spencer, J. Knight, M.E. Weale, M.H. Allen, A. Barton, G. Band, C. Bellenguez,
1093 J.G. Bergboer, J.M. Blackwell, E. Bramon, S.J. Bumpstead, J.P. Casas, M.J. Cork, A. Corvin, P.
1094 Deloukas, A. Dilthey, A. Duncanson, S. Edkins, X. Estivill, O. Fitzgerald, C. Freeman, E. Giardina, E.
1095 Gray, A. Hofer, U. Huffmeier, S.E. Hunt, A.D. Irvine, J. Jankowski, B. Kirby, C. Langford, J. Lascorz,

1096 J. Leman, S. Leslie, L. Mallbris, H.S. Markus, C.G. Mathew, W.H. McLean, R. McManus, R. Mossner,
1097 L. Moutsianas, A.T. Naluai, F.O. Nestle, G. Novelli, A. Onoufriadis, C.N. Palmer, C. Perricone, M.
1098 Pirinen, R. Plomin, S.C. Potter, R.M. Pujol, A. Rautanen, E. Riveira-Munoz, A.W. Ryan, W.
1099 Salmhofer, L. Samuelsson, S.J. Sawcer, J. Schalkwijk, C.H. Smith, M. Stahle, Z. Su, R. Tazi-Ahnini, H.
1100 Traupe, A.C. Viswanathan, R.B. Warren, W. Weger, K. Wolk, N. Wood, J. Worthington, H.S. Young,
1101 P.L. Zeeuwen, A. Hayday, A.D. Burden, C.E. Griffiths, J. Kere, A. Reis, G. McVean, D.M. Evans, M.A.
1102 Brown, J.N. Barker, L. Peltonen, P. Donnelly, and R.C. Trembath. 2010. A genome-wide association
1103 study identifies new psoriasis susceptibility loci and an interaction between HLA-C and ERAP1. *Nat*
1104 *Genet* 42:985-990.
1105 Strugnell, R., G. Dougan, S. Chatfield, I. Charles, N. Fairweather, J. Tite, J.L. Li, J. Beesley, and M. Roberts.
1106 1992. Characterization of a Salmonella typhimurium aro vaccine strain expressing the P.69 antigen
1107 of Bordetella pertussis. *Infect Immun* 60:3994-4002.
1108 Su, L., B. Quade, H. Wang, L. Sun, X. Wang, and J. Rizo. 2014. A plug release mechanism for membrane
1109 permeation by MLKL. *Structure* 22:1489-1500.
1110 Sun, L., H. Wang, Z. Wang, S. He, S. Chen, D. Liao, L. Wang, J. Yan, W. Liu, X. Lei, and X. Wang. 2012. Mixed
1111 lineage kinase domain-like protein mediates necrosis signaling downstream of RIP3 kinase. *Cell*
1112 148:213-227.
1113 Tanzer, M.C., I. Matti, J.M. Hildebrand, S.N. Young, A. Wardak, A. Tripaydonis, E.J. Petrie, A.L. Mildenhall,
1114 D.L. Vaux, J.E. Vince, P.E. Czabotar, J. Silke, and J.M. Murphy. 2016. Evolutionary divergence of the
1115 necroptosis effector MLKL. *Cell Death Differ* 23:1185-1197.
1116 Thapa, R.J., S. Nogusa, P. Chen, J.L. Maki, A. Lerro, M. Andrake, G.F. Rall, A. Degterev, and S. Balachandran.
1117 2013. Interferon-induced RIP1/RIP3-mediated necrosis requires PKR and is licensed by FADD and
1118 caspases. *Proceedings of the National Academy of Sciences of the United States of America*
1119 110:E3109-3118.
1120 Tovey Crutchfield, E.C., S.E. Garnish, and J.M. Hildebrand. 2021. The Role of the Key Effector of
1121 Necroptotic Cell Death, MLKL, in Mouse Models of Disease. *Biomolecules* 11:
1122 Tsoi, L.C., S.L. Spain, J. Knight, E. Ellinghaus, P.E. Stuart, F. Capon, J. Ding, Y. Li, T. Tejasvi, J.E. Gudjonsson,
1123 H.M. Kang, M.H. Allen, R. McManus, G. Novelli, L. Samuelsson, J. Schalkwijk, M. Stahle, A.D.
1124 Burden, C.H. Smith, M.J. Cork, X. Estivill, A.M. Bowcock, G.G. Krueger, W. Weger, J. Worthington,
1125 R. Tazi-Ahnini, F.O. Nestle, A. Hayday, P. Hoffmann, J. Winkelmann, C. Wijmenga, C. Langford, S.
1126 Edkins, R. Andrews, H. Blackburn, A. Strange, G. Band, R.D. Pearson, D. Vukcevic, C.C. Spencer, P.
1127 Deloukas, U. Mrowietz, S. Schreiber, S. Weidinger, S. Koks, K. Kingo, T. Esko, A. Metspalu, H.W.
1128 Lim, J.J. Voorhees, M. Weichenthal, H.E. Wichmann, V. Chandran, C.F. Rosen, P. Rahman, D.D.
1129 Gladman, C.E. Griffiths, A. Reis, J. Kere, P. Collaborative Association Study of, C. Genetic Analysis
1130 of Psoriasis, E. Psoriasis Association Genetics, C. Wellcome Trust Case Control, R.P. Nair, A. Franke,
1131 J.N. Barker, G.R. Abecasis, J.T. Elder, and R.C. Trembath. 2012. Identification of 15 new psoriasis
1132 susceptibility loci highlights the role of innate immunity. *Nat Genet* 44:1341-1348.
1133 Upton, J.W., W.J. Kaiser, and E.S. Mocarski. 2010. Virus inhibition of RIP3-dependent necrosis. *Cell Host*
1134 *Microbe* 7:302-313.
1135 Vince, J.E., W.W. Wong, N. Khan, R. Feltham, D. Chau, A.U. Ahmed, C.A. Benetatos, S.K. Chunduru, S.M.
1136 Condon, M. McKinlay, R. Brink, M. Leverkus, V. Tergaonkar, P. Schneider, B.A. Callus, F. Koentgen,
1137 D.L. Vaux, and J. Silke. 2007. IAP antagonists target cIAP1 to induce TNFalpha-dependent
1138 apoptosis. *Cell* 131:682-693.
1139 Wang, B., S. Bao, Z. Zhang, X. Zhou, J. Wang, Y. Fan, Y. Zhang, Y. Li, L. Chen, Y. Jia, J. Li, M. Li, W. Zheng, N.
1140 Mu, L. Wang, Z. Yu, D.S.M. Wong, Y. Zhang, J. Kwan, H. Ka-Fung Mak, A. Ambalavanan, S. Zhou,
1141 W. Cai, J. Zheng, S. Huang, G.A. Rouleau, W. Yang, E. Rogaeva, X. Ma, P. St George-Hyslop, L.W.
1142 Chu, and Y.Q. Song. 2018. A rare variant in MLKL confers susceptibility to ApoE varepsilon4-

1143 negative Alzheimer's disease in Hong Kong Chinese population. *Neurobiol Aging* 68:160 e161-160
1144 e167.
1145 Wang, H., L. Sun, L. Su, J. Rizo, L. Liu, L.F. Wang, F.S. Wang, and X. Wang. 2014a. Mixed lineage kinase
1146 domain-like protein MLKL causes necrotic membrane disruption upon phosphorylation by RIP3.
1147 *Mol Cell* 54:133-146.
1148 Wang, H., H. Yang, C.S. Shivalila, M.M. Dawlaty, A.W. Cheng, F. Zhang, and R. Jaenisch. 2013. One-step
1149 generation of mice carrying mutations in multiple genes by CRISPR/Cas-mediated genome
1150 engineering. *Cell* 153:910-918.
1151 Wang, H.Y., L.M. Sun, L.J. Su, J. Rizo, L. Liu, L.F. Wang, F.S. Wang, and X.D. Wang. 2014b. Mixed Lineage
1152 Kinase Domain-like Protein MLKL Causes Necrotic Membrane Disruption upon Phosphorylation
1153 by RIP3. *Molecular Cell* 54:133-146.
1154 Weir, A., S. Hughes, M. Rashidi, J.M. Hildebrand, and J.E. Vince. 2021. Necroptotic movers and shakers:
1155 cell types, inflammatory drivers and diseases. *Curr Opin Immunol* 68:83-97.
1156 Wemyss, M.A., and J.S. Pearson. 2019. Host Cell Death Responses to Non-typhoidal Salmonella Infection.
1157 *Front Immunol* 10:1758.
1158 Werren, E.A., O. Garcia, and A.W. Bigham. 2021. Identifying adaptive alleles in the human genome: from
1159 selection mapping to functional validation. *Hum Genet* 140:241-276.
1160 Wu, J., Z. Huang, J. Ren, Z. Zhang, P. He, Y. Li, J. Ma, W. Chen, Y. Zhang, X. Zhou, Z. Yang, S.Q. Wu, L. Chen,
1161 and J. Han. 2013. Mlkl knockout mice demonstrate the indispensable role of Mlkl in necroptosis.
1162 *Cell research* 23:994-1006.
1163 Yan, B., L. Liu, S. Huang, Y. Ren, H. Wang, Z. Yao, L. Li, S. Chen, X. Wang, and Z. Zhang. 2017. Discovery of
1164 a new class of highly potent necroptosis inhibitors targeting the mixed lineage kinase domain-like
1165 protein. *Chem Commun (Camb)* 53:3637-3640.
1166 Yin, X., H.Q. Low, L. Wang, Y. Li, E. Ellinghaus, J. Han, X. Estivill, L. Sun, X. Zuo, C. Shen, C. Zhu, A. Zhang, F.
1167 Sanchez, L. Padyukov, J.J. Catanese, G.G. Krueger, K.C. Duffin, S. Mucha, M. Weichenthal, S.
1168 Weidinger, W. Lieb, J.N. Foo, Y. Li, K. Sim, H. Liany, I. Irwan, Y. Teo, C.T. Theng, R. Gupta, A.
1169 Bowcock, P.L. De Jager, A.A. Qureshi, P.I. de Bakker, M. Seielstad, W. Liao, M. Stahle, A. Franke, X.
1170 Zhang, and J. Liu. 2015. Genome-wide meta-analysis identifies multiple novel associations and
1171 ethnic heterogeneity of psoriasis susceptibility. *Nat Commun* 6:6916.
1172 Yoon, S., K. Bogdanov, and D. Wallach. 2022. Site-specific ubiquitination of MLKL targets it to endosomes
1173 and targets Listeria and Yersinia to the lysosomes. *Cell Death Differ*
1174 Zhang, J., T. Jin, I. Aksentijevich, and Q. Zhou. 2021. RIPK1-Associated Inborn Errors of Innate Immunity.
1175 *Front Immunol* 12:676946.
1176 Zhao, J., S. Jitkaew, Z. Cai, S. Choksi, Q. Li, J. Luo, and Z.G. Liu. 2012. Mixed lineage kinase domain-like is a
1177 key receptor interacting protein 3 downstream component of TNF-induced necrosis. *Proceedings*
1178 *of the National Academy of Sciences of the United States of America* 109:5322-5327.
1179 Zhu, X., N. Yang, Y. Yang, F. Yuan, D. Yu, Y. Zhang, Z. Shu, N. Nan, H. Hu, X. Liu, S. Chen, L. Sun, and H.
1180 Wang. 2022. Spontaneous necroptosis and autoinflammation are blocked by an inhibitory
1181 phosphorylation on MLKL during neonatal development. *Cell Res* 32:407-410.

1182

1183

Figure 1

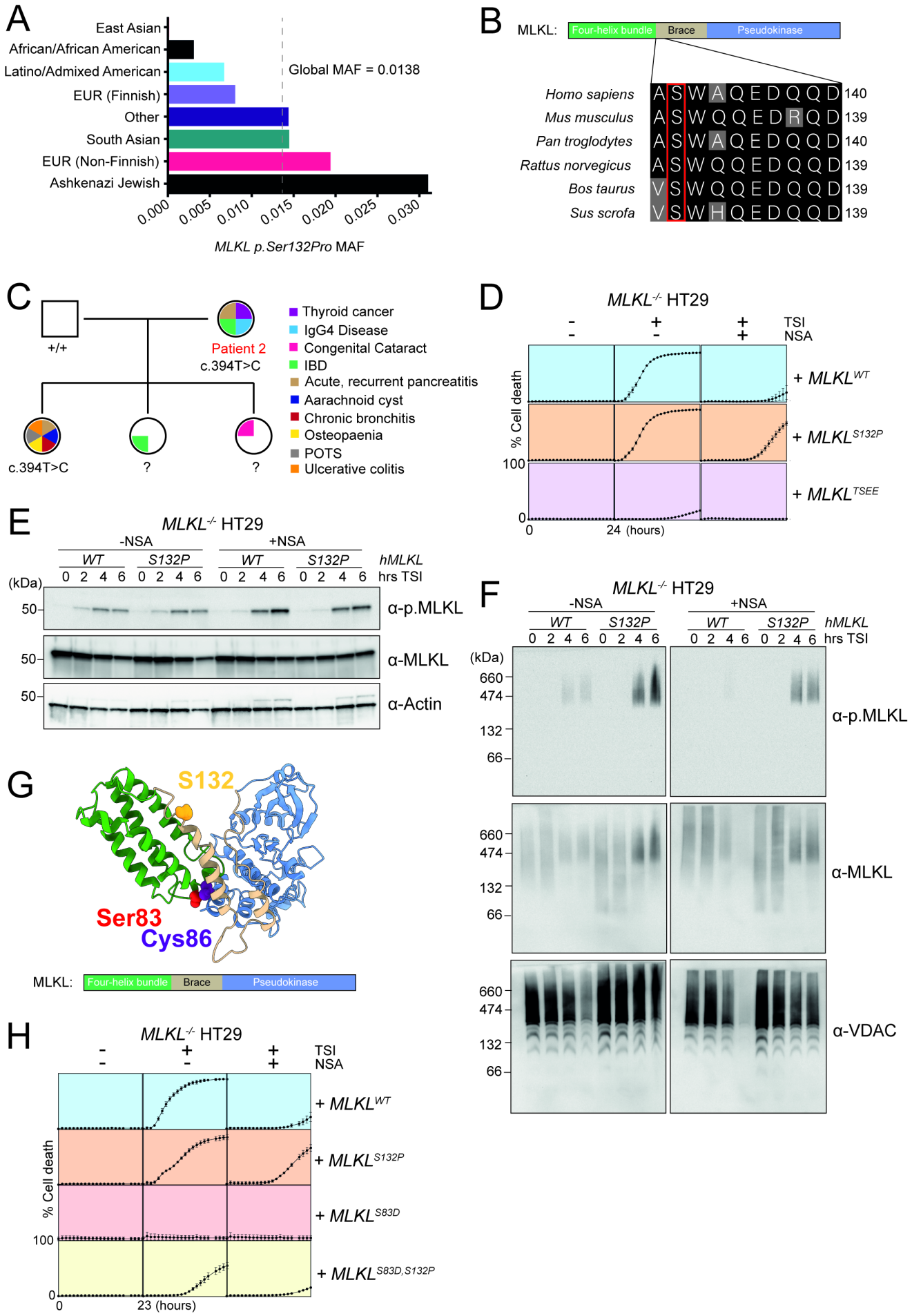
A
East Asian
African/African American
Latino/Admixed American
EUR (Finnish)
Other
South Asian
EUR (Non-Finnish)
Ashkenazi Jewish
Global MAF = 0.0138
0.000
0.005
0.010
0.015
0.020
0.025
0.030
MLKL p.Ser132Pro MAF
B
MLKL:
Four-helix bundle
Brace
Pseudokinase
Homo sapiens
Mus musculus
Pan troglodytes
Rattus norvegicus
Bos taurus
Sus scrofa
140
139
C
+/+
Patient 2
c.394T>C
c.394T>C
?
?
Thyroid cancer
IgG4 Disease
Congenital Cataract
IBD
Acute, recurrent pancreatitis
Aarachnoid cyst
Chronic bronchitis
Osteopaenia
POTS
Ulcerative colitis
D
MLKL-/- HT29
TSI
NSA
% Cell death
100
0
0
24 (hours)
+ MLKLWT
+ MLKLS132P
+ MLKLTSEE
E
MLKL-/- HT29
-NSA
+NSA
WT
S132P
hMLKL
hrs TSI
(kDa)
50
α-p.MLKL
α-MLKL
α-Actin
F
MLKL-/- HT29
-NSA
+NSA
WT
S132P
hMLKL
hrs TSI
(kDa)
660
474
132
66
α-p.MLKL
α-MLKL
α-VDAC
G
S132
Ser83
Cys86
MLKL:
Four-helix bundle
Brace
Pseudokinase
H
MLKL-/- HT29
TSI
NSA
% Cell death
100
0
0
23 (hours)
+ MLKLWT
+ MLKLS132P
+ MLKLS83D
+ MLKLS83D,S132P

Figure 2

A

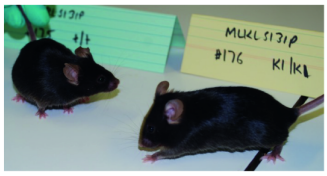

B

Mlkl$^{WT/S131P}$ X *Mlkl*$^{WT/S131P}$	
Number of litters	10
Number of offspring (P21)	80

G/type of offspring	Obs.	Exp.
Mlkl$^{WT/WT}$	24	20
Mlkl$^{WT/S131P}$	35	40
Mlkl$^{S131P/S131P}$	21	20

C

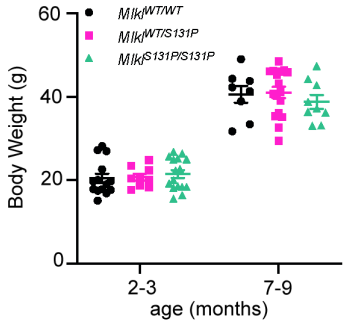

D

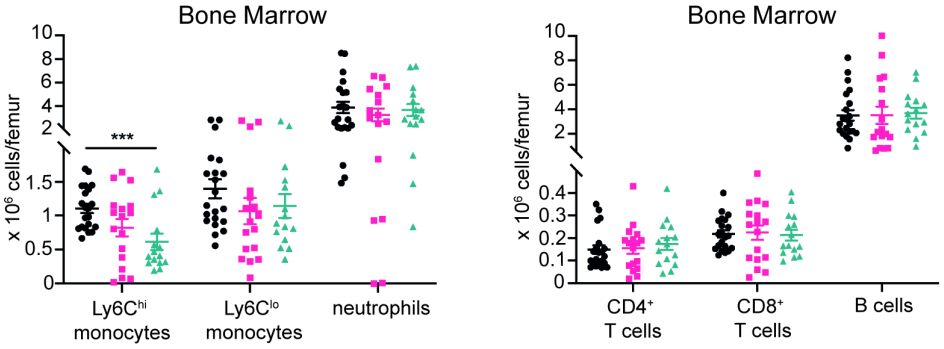

E

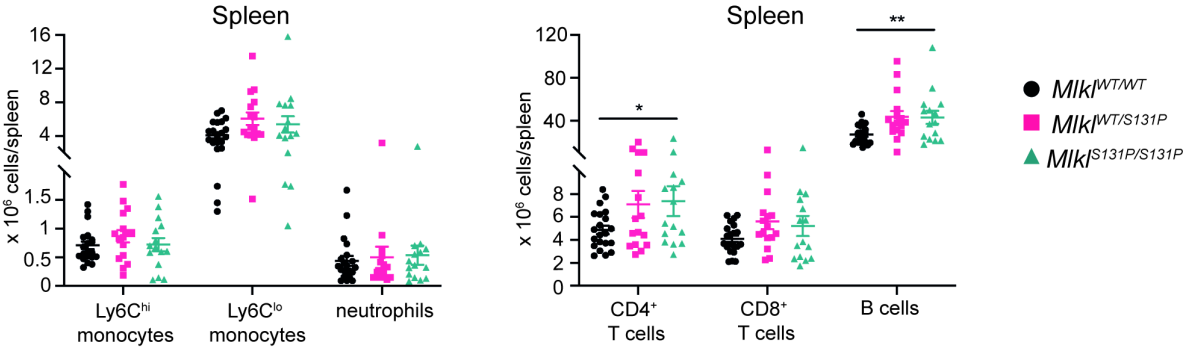

F

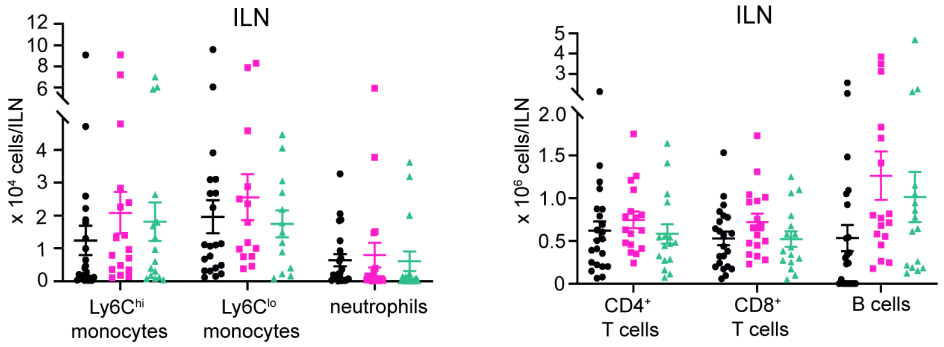

G

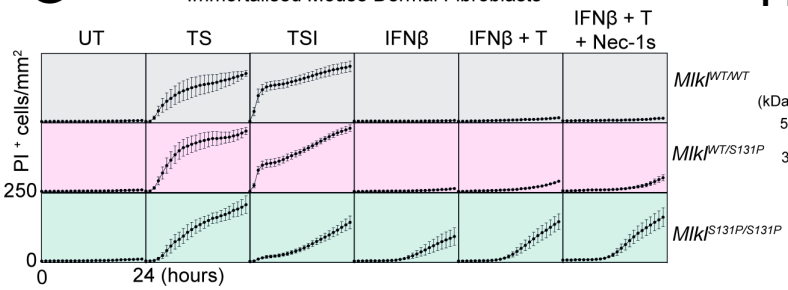

H

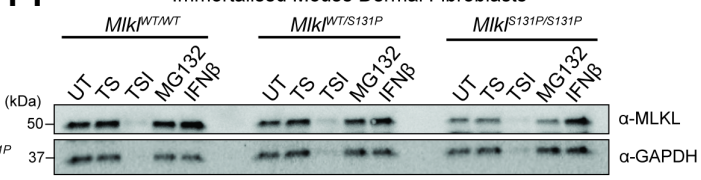

Figure 3

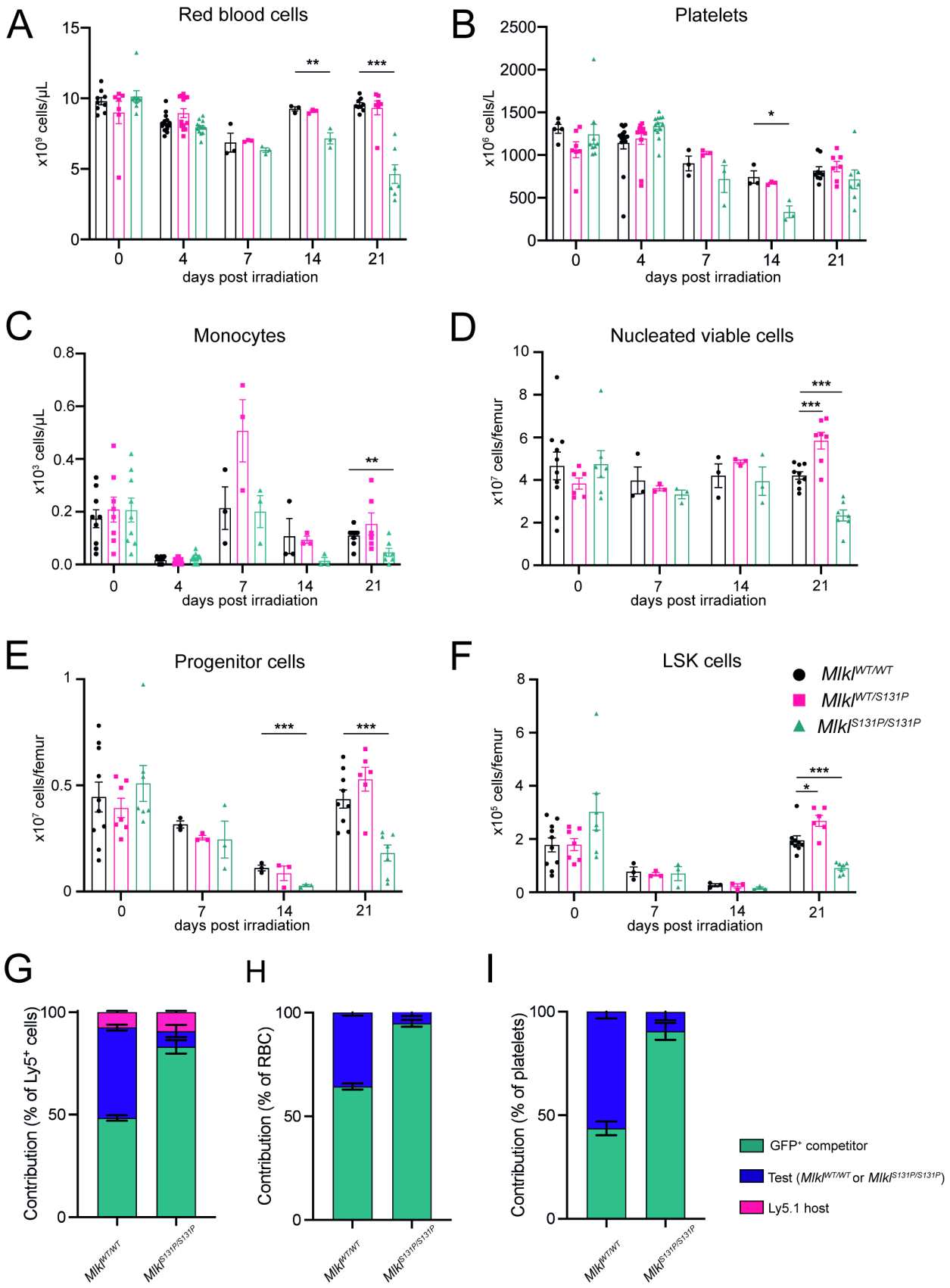
A
Red blood cells
x10⁹ cells/μL
days post irradiation
B
Platelets
x10⁶ cells/L
days post irradiation
C
Monocytes
x10³ cells/μL
days post irradiation
D
Nucleated viable cells
x10⁷ cells/femur
days post irradiation
E
Progenitor cells
x10⁷ cells/femur
days post irradiation
F
LSK cells
x10⁵ cells/femur
days post irradiation
Mlkl WT/WT
Mlkl WT/S131P
Mlkl S131P/S131P
G
H
I
Contribution (% of Ly5⁺ cells)
Contribution (% of RBC)
Contribution (% of platelets)
GFP⁺ competitor
Test (Mlkl WT/WT or Mlkl S131P/S131P)
Ly5.1 host

Figure 4

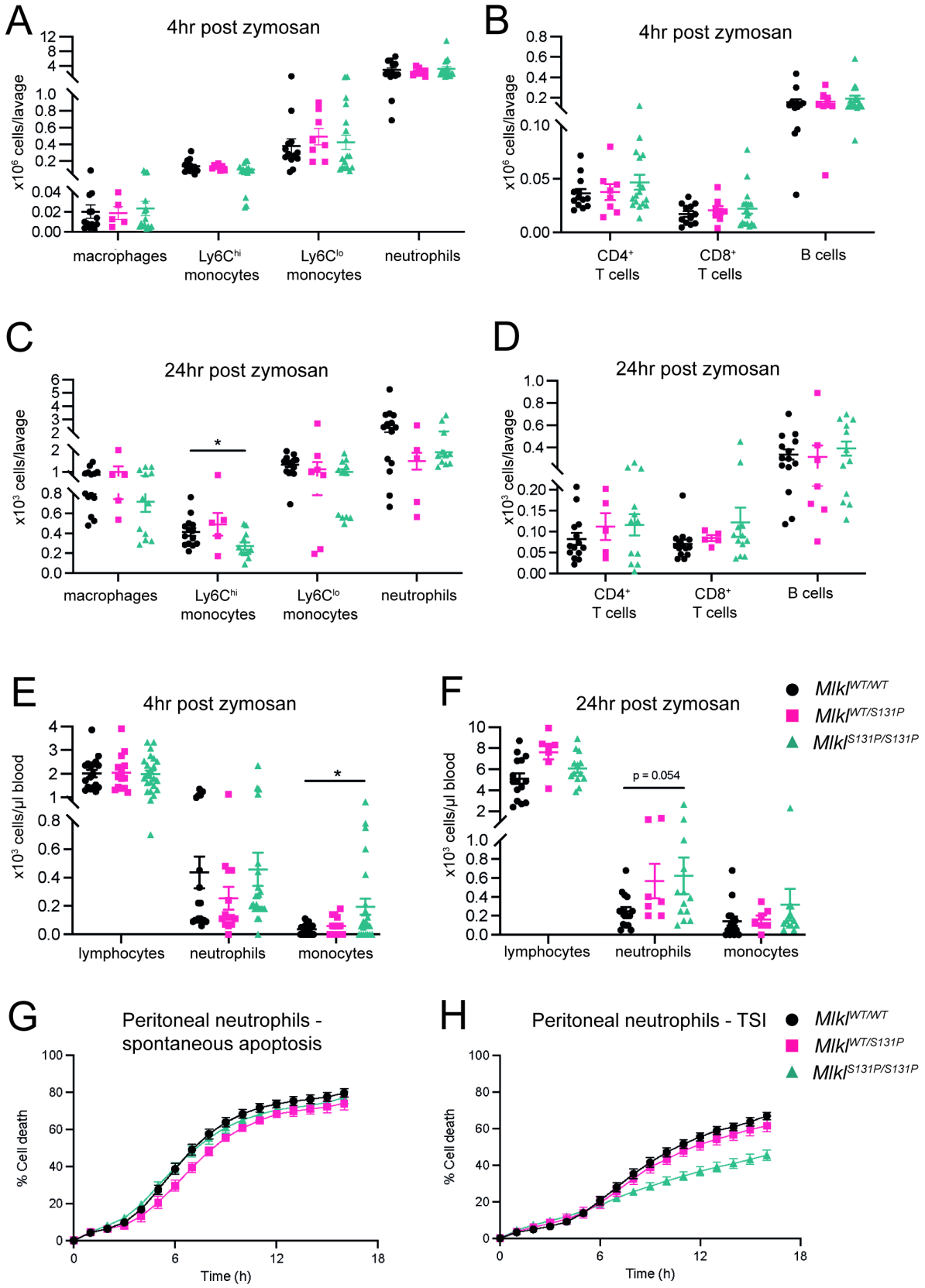
A
4hr post zymosan
x10⁶ cells/lavage
macrophages
Ly6C^hi monocytes
Ly6C^lo monocytes
neutrophils
B
4hr post zymosan
x10⁶ cells/lavage
CD4⁺ T cells
CD8⁺ T cells
B cells
C
24hr post zymosan
x10³ cells/lavage
*
macrophages
Ly6C^hi monocytes
Ly6C^lo monocytes
neutrophils
D
24hr post zymosan
x10³ cells/lavage
CD4⁺ T cells
CD8⁺ T cells
B cells
E
4hr post zymosan
x10³ cells/µl blood
*
lymphocytes
neutrophils
monocytes
F
24hr post zymosan
x10³ cells/µl blood
p = 0.054
lymphocytes
neutrophils
monocytes
Mlkl^WT/WT
Mlkl^WT/S131P
Mlkl^S131P/S131P
G
Peritoneal neutrophils - spontaneous apoptosis
% Cell death
Time (h)
H
Peritoneal neutrophils - TSI
% Cell death
Time (h)
Mlkl^WT/WT
Mlkl^WT/S131P
Mlkl^S131P/S131P

Figure 5

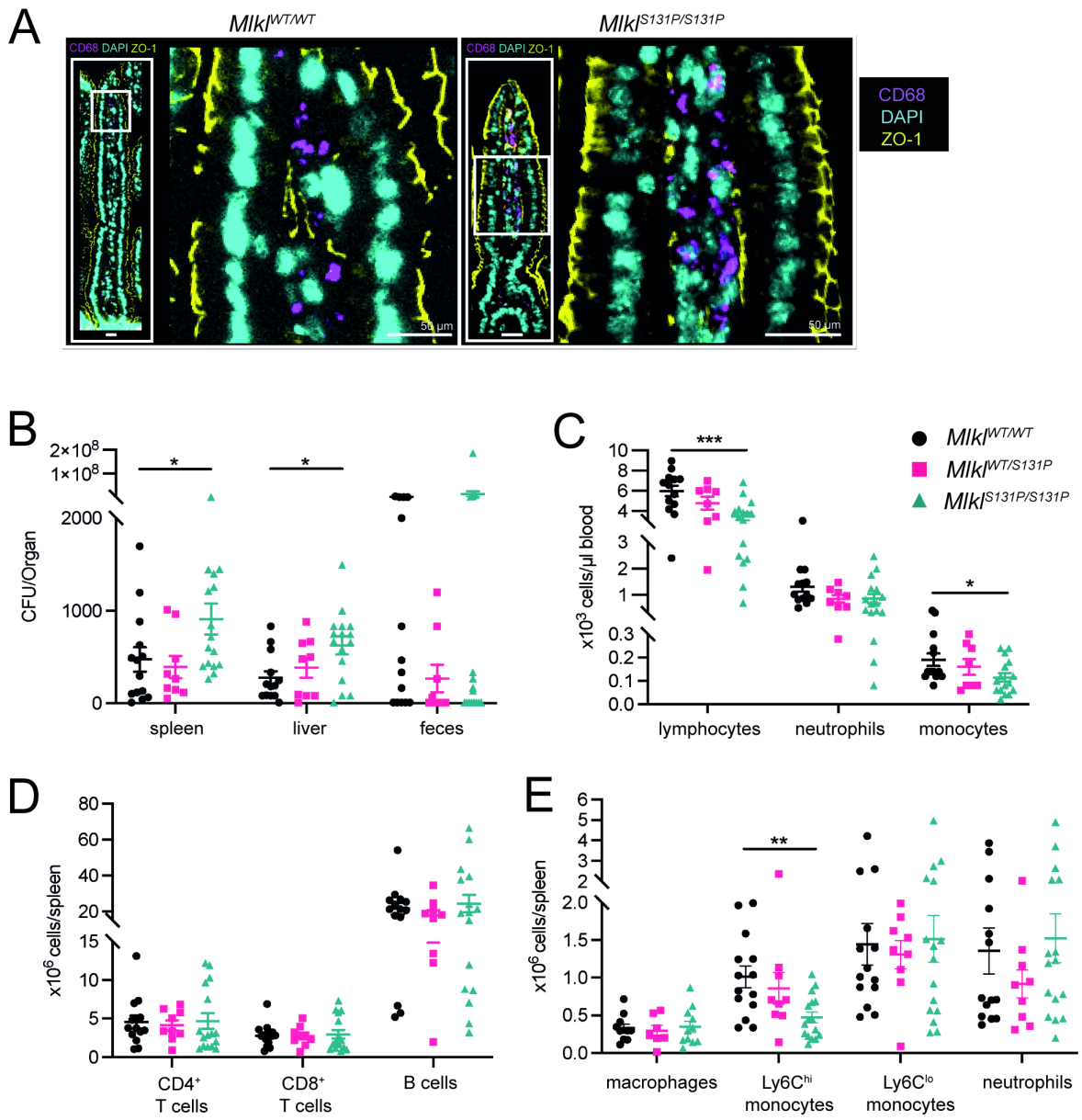
A
Mlkl WT/WT
Mlkl S131P/S131P
CD68 DAPI ZO-1
50 µm
B
CFU/Organ
spleen
liver
feces
C
x10³ cells/µl blood
lymphocytes
neutrophils
monocytes
Mlkl WT/WT
Mlkl WT/S131P
Mlkl S131P/S131P
D
x10⁶ cells/spleen
CD4⁺ T cells
CD8⁺ T cells
B cells
E
x10⁶ cells/spleen
macrophages
Ly6C hi monocytes
Ly6C lo monocytes
neutrophils

Supplementary Figure 1

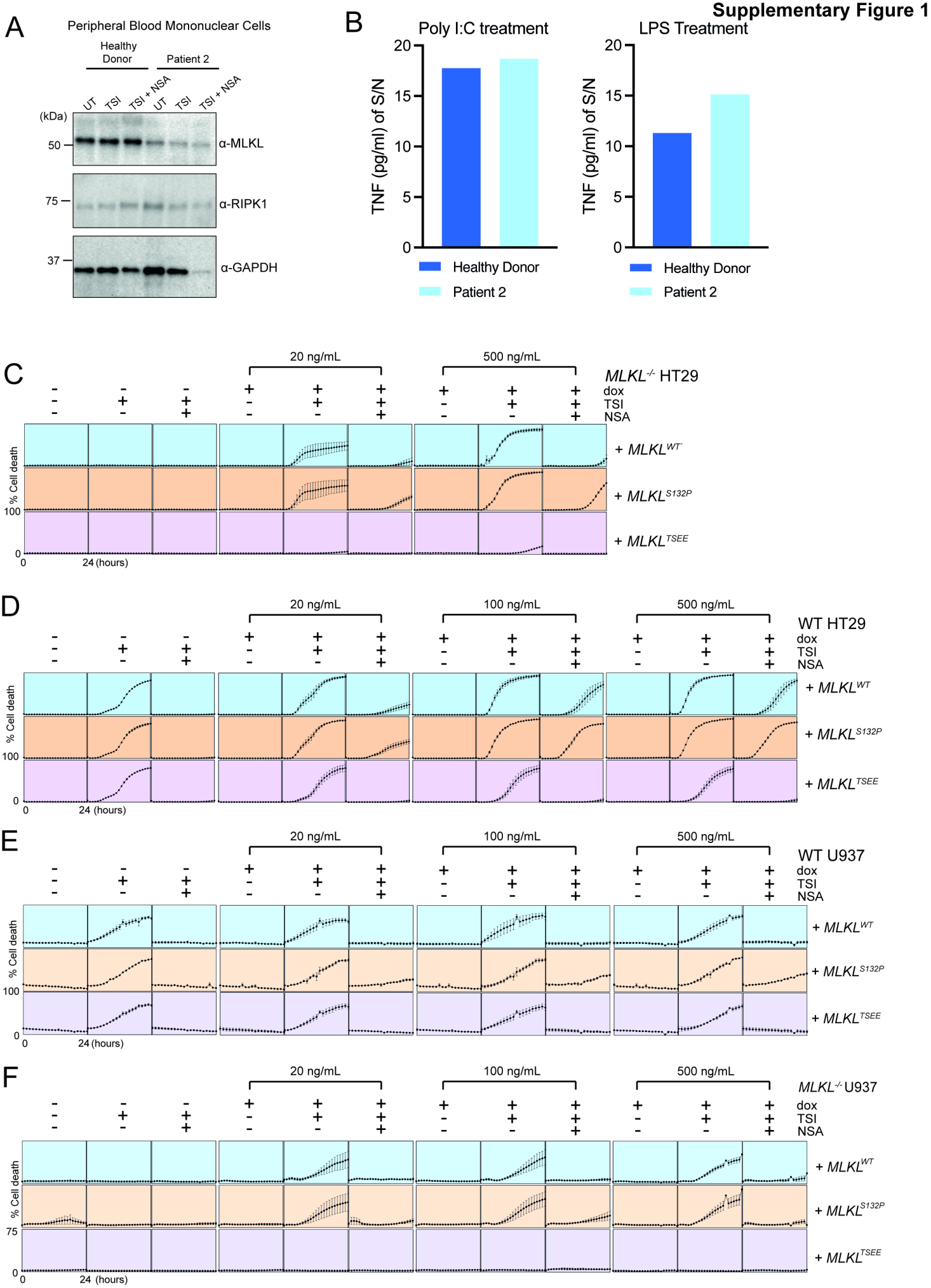

Supplementary Figure 1 cont.

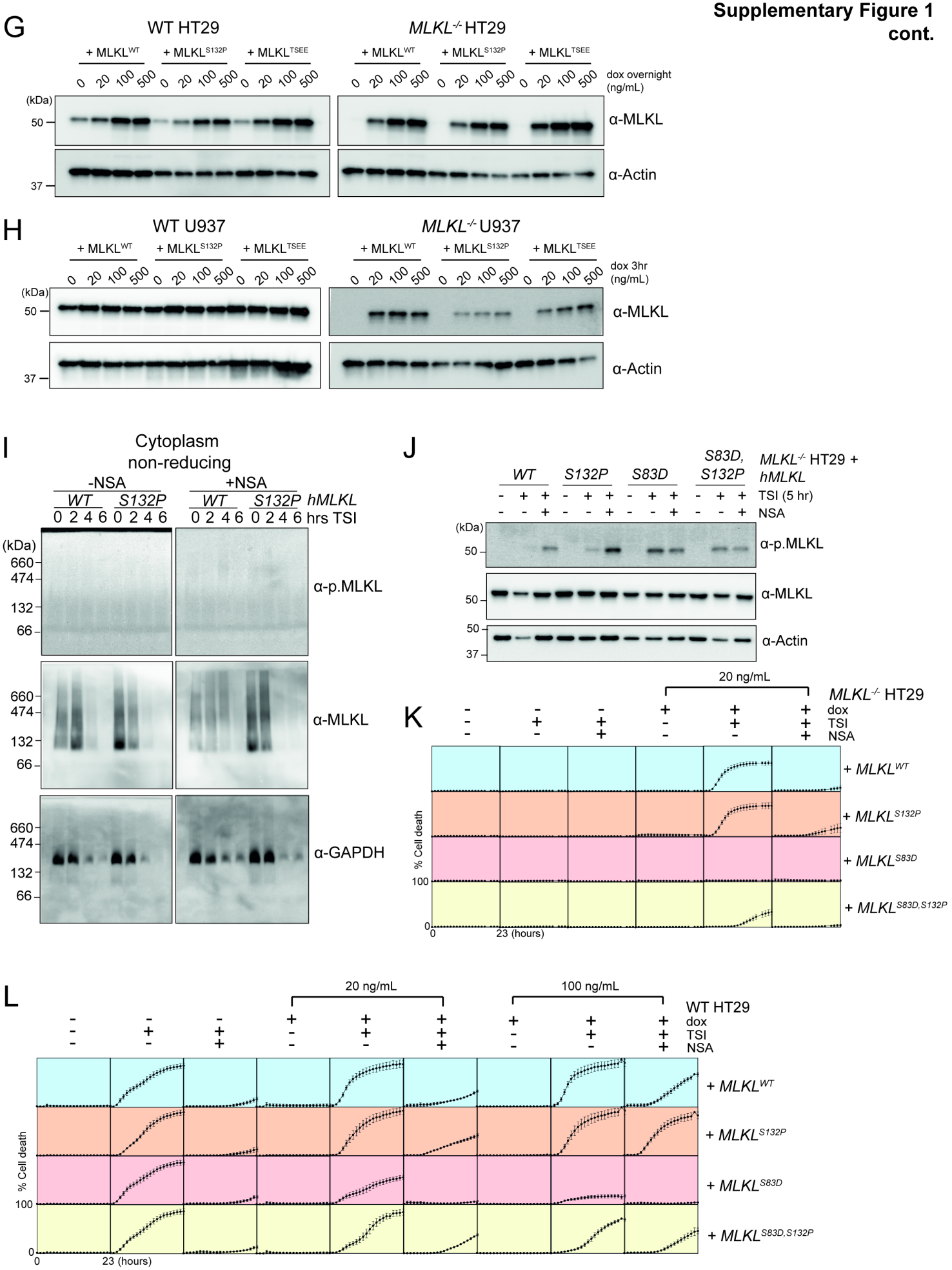

Supplementary Figure 2

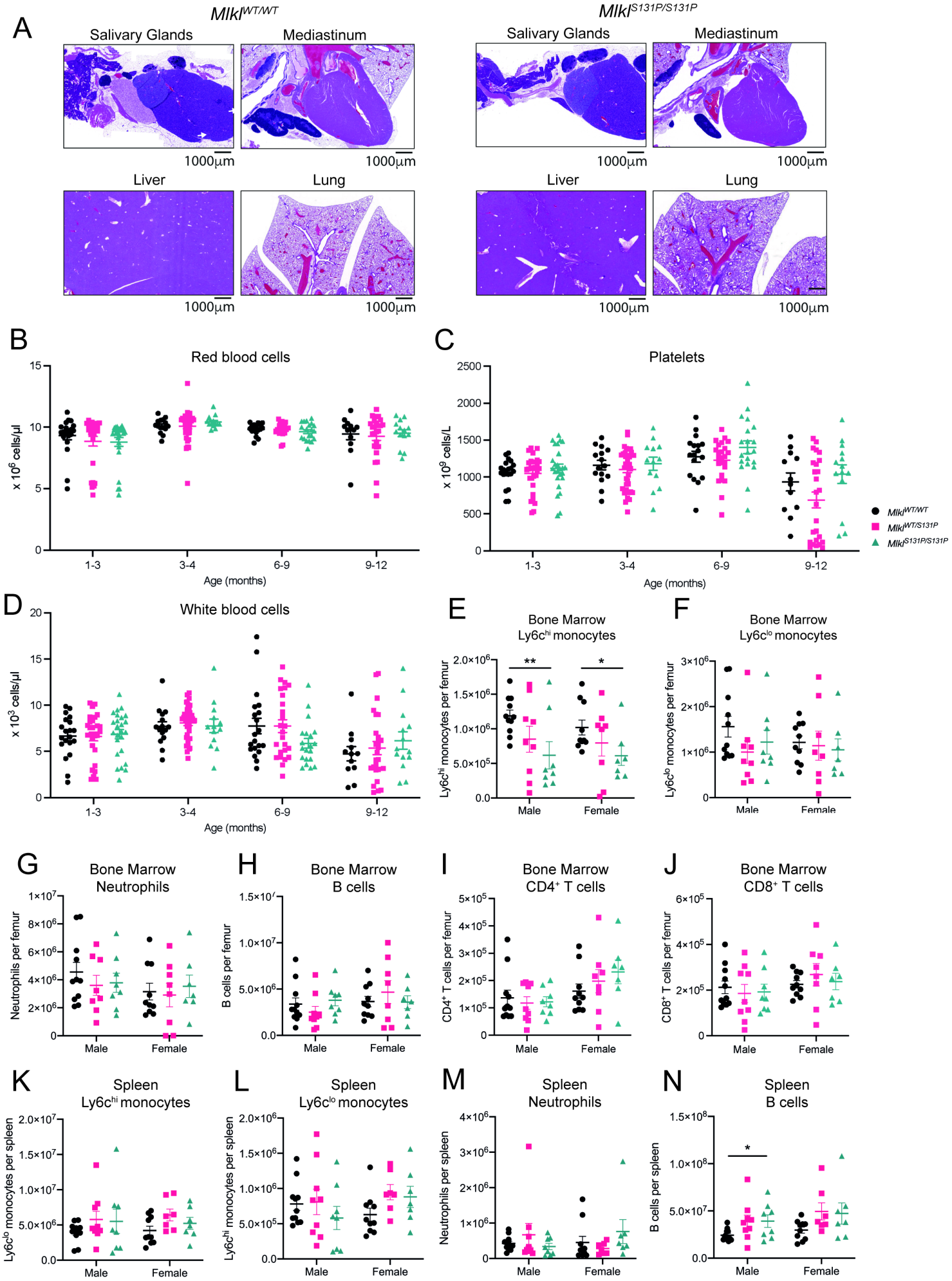

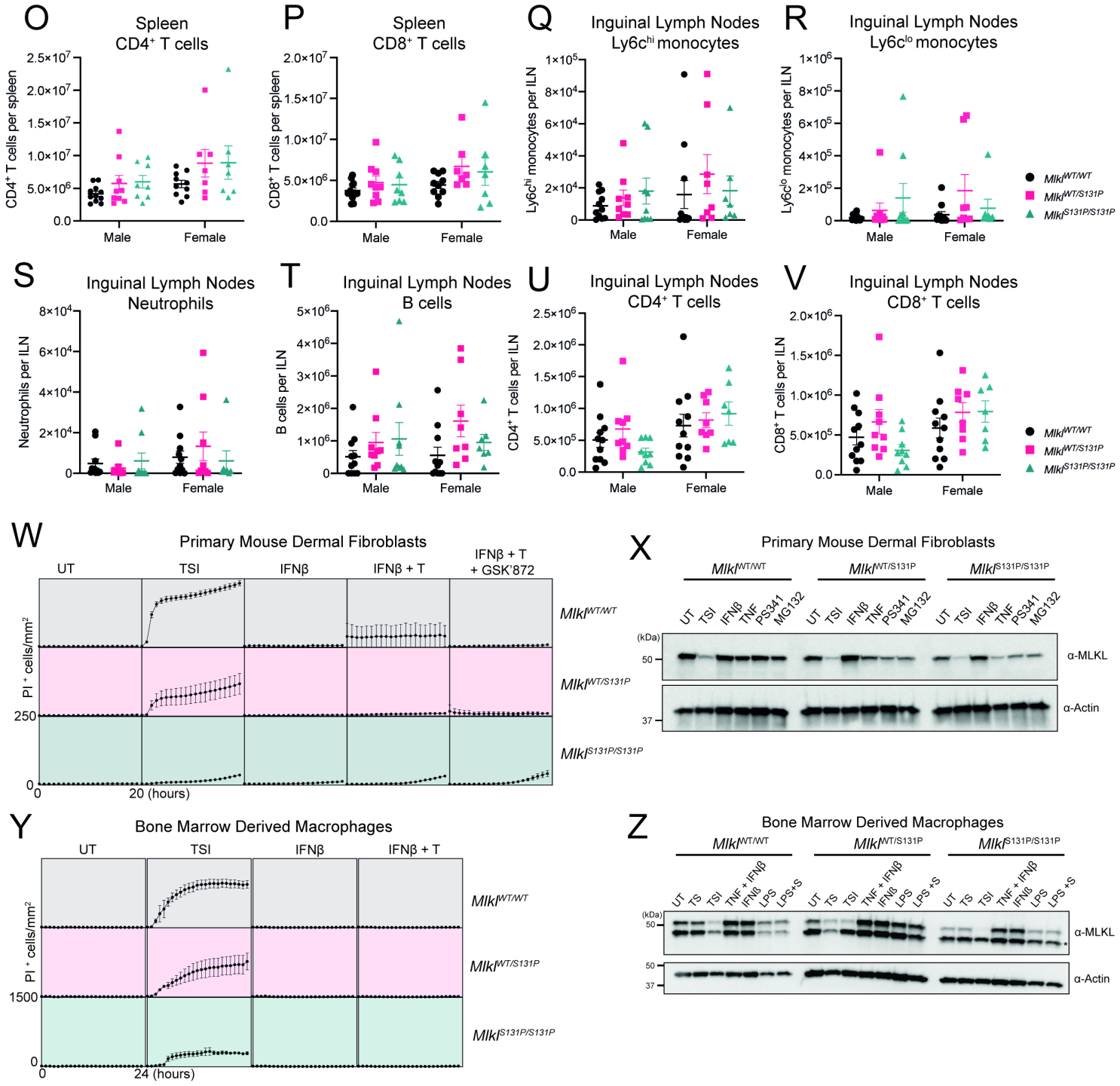
O
Spleen
CD4+ T cells
CD4+ T cells per spleen
2.5×10^7
2.0×10^7
1.5×10^7
1.0×10^7
5.0×10^6
0.0
Male
Female
P
Spleen
CD8+ T cells
CD8+ T cells per spleen
2.0×10^7
1.5×10^7
1.0×10^7
5.0×10^6
0.0
Male
Female
Q
Inguinal Lymph Nodes
Ly6chi monocytes
Ly6chi monocytes per ILN
1×10^5
8×10^4
6×10^4
4×10^4
2×10^4
0
Male
Female
R
Inguinal Lymph Nodes
Ly6clo monocytes
Ly6clo monocytes per ILN
1×10^6
8×10^5
6×10^5
4×10^5
2×10^5
0
Male
Female
Mlkl WT/WT
Mlkl WT/S131P
Mlkl S131P/S131P
S
Inguinal Lymph Nodes
Neutrophils
Neutrophils per ILN
8×10^4
6×10^4
4×10^4
2×10^4
0
Male
Female
T
Inguinal Lymph Nodes
B cells
B cells per ILN
5×10^6
4×10^6
3×10^6
2×10^6
1×10^6
0
Male
Female
U
Inguinal Lymph Nodes
CD4+ T cells
CD4+ T cells per ILN
2.5×10^6
2.0×10^6
1.5×10^6
1.0×10^6
5.0×10^5
0.0
Male
Female
V
Inguinal Lymph Nodes
CD8+ T cells
CD8+ T cells per ILN
2.0×10^6
1.5×10^6
1.0×10^6
5.0×10^5
0.0
Male
Female
Mlkl WT/WT
Mlkl WT/S131P
Mlkl S131P/S131P
W
Primary Mouse Dermal Fibroblasts
UT
TSI
IFNβ
IFNβ + T
IFNβ + T + GSK'872
PI + cells/mm2
250
0
0
20 (hours)
Mlkl WT/WT
Mlkl WT/S131P
Mlkl S131P/S131P
X
Primary Mouse Dermal Fibroblasts
Mlkl WT/WT
Mlkl WT/S131P
Mlkl S131P/S131P
UT
TSI
IFNβ
TNF
PS341
MG132
(kDa)
50
37
α-MLKL
α-Actin
Y
Bone Marrow Derived Macrophages
UT
TSI
IFNβ
IFNβ + T
PI + cells/mm2
1500
0
0
24 (hours)
Mlkl WT/WT
Mlkl WT/S131P
Mlkl S131P/S131P
Z
Bone Marrow Derived Macrophages
Mlkl WT/WT
Mlkl WT/S131P
Mlkl S131P/S131P
UT
TS
TSI
TNF + IFNβ
IFNβ
LPS
LPS+S
(kDa)
50
37
α-MLKL
α-Actin

Supplementary Figure 3

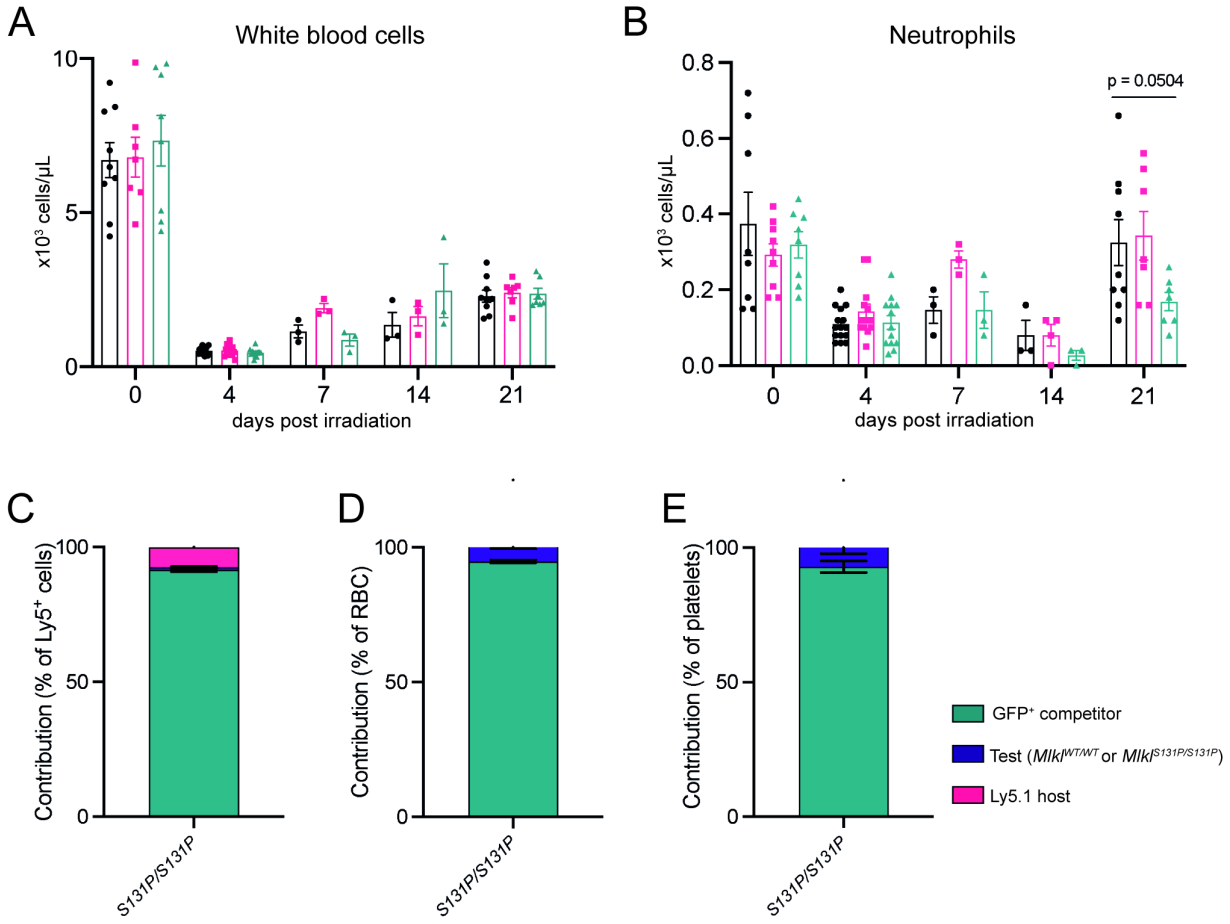

Supplementary Figure 4

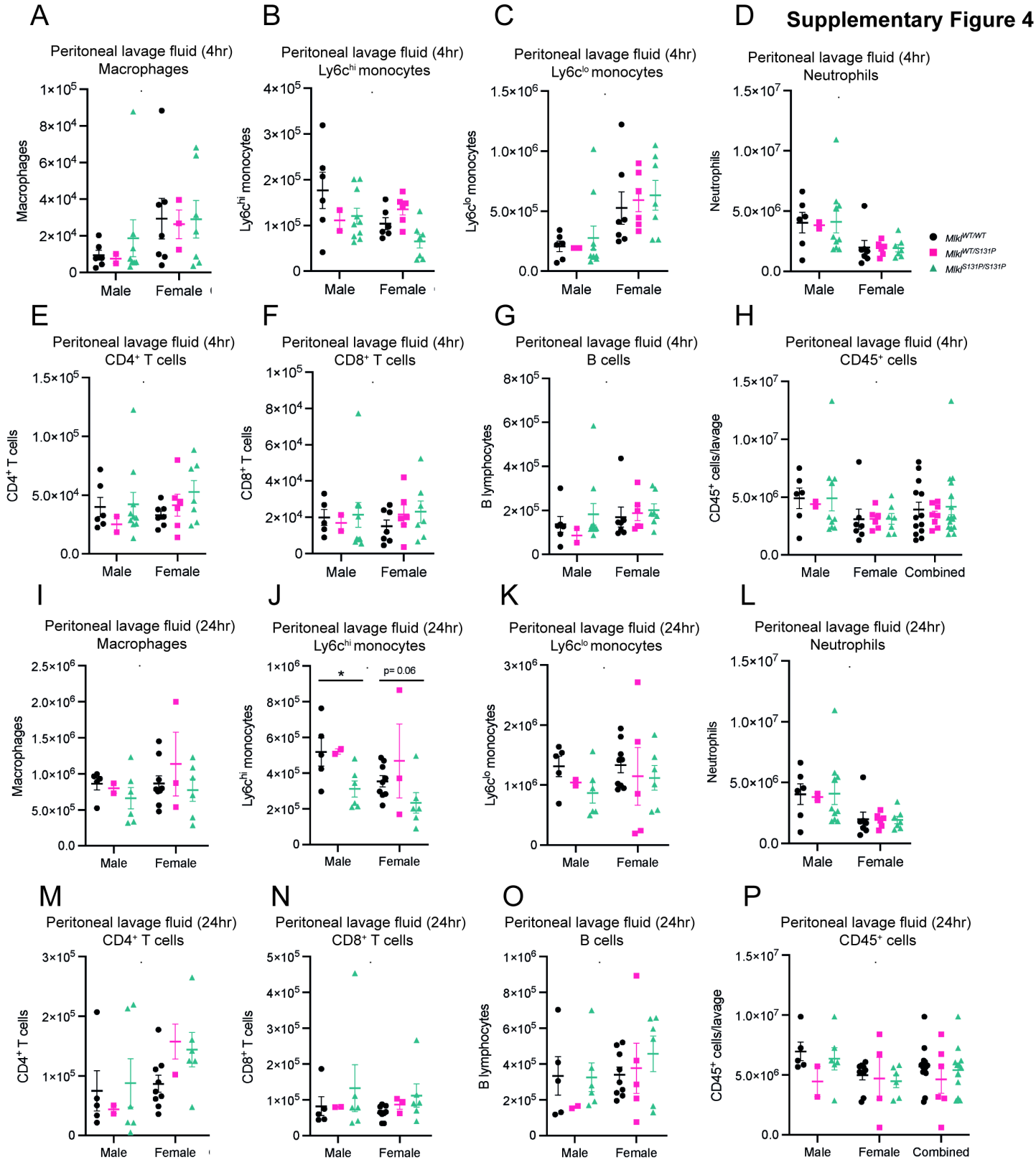

Supplementary Figure 4 cont.

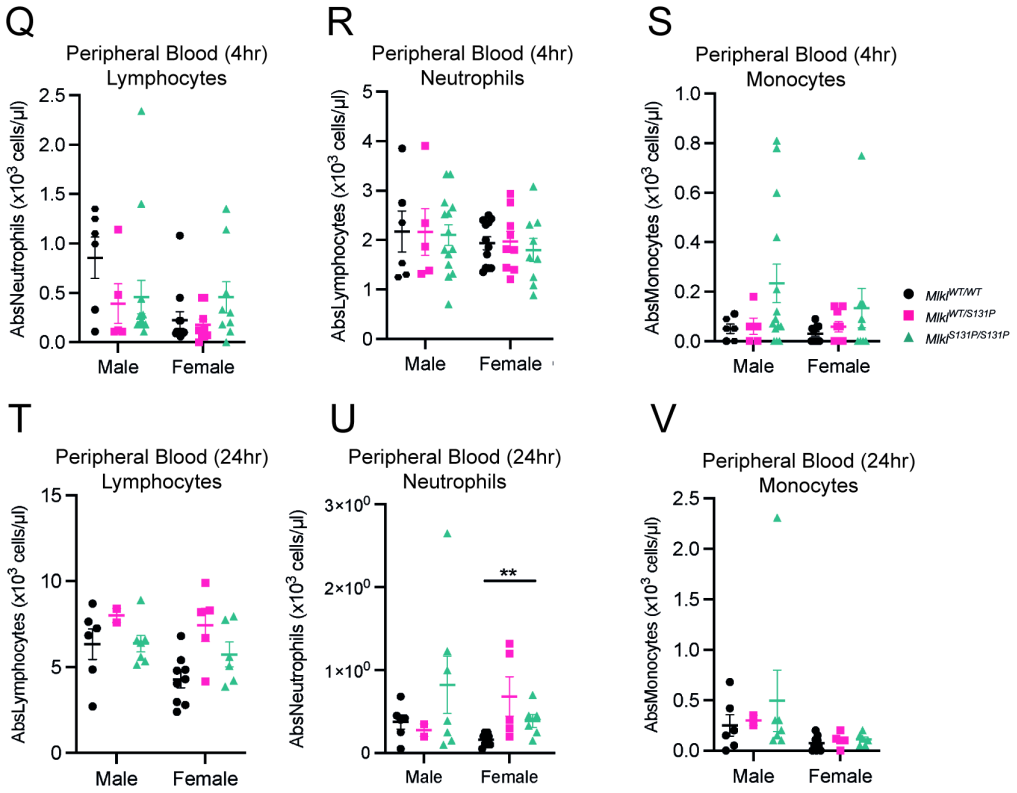

Supplementary Figure 5

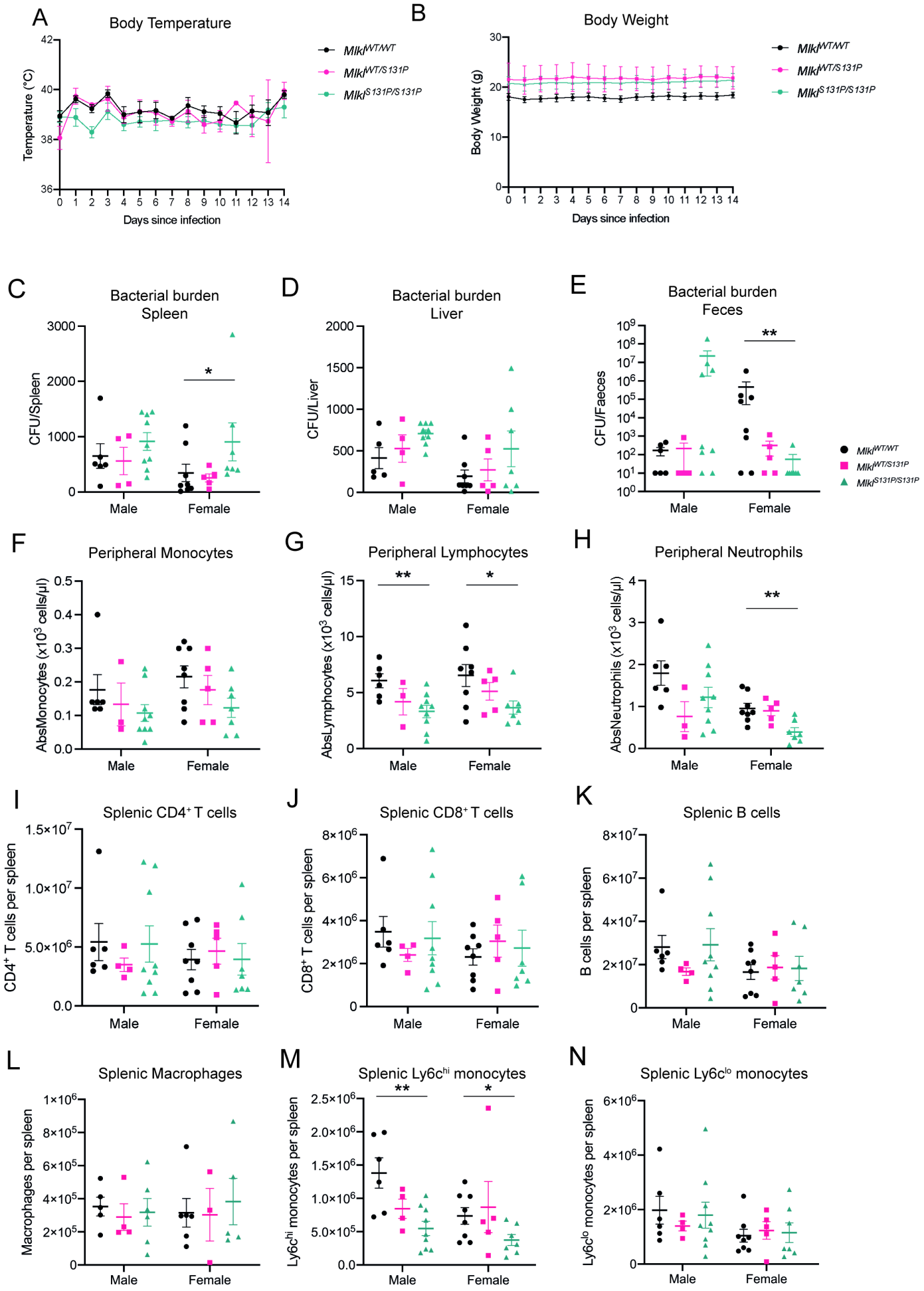
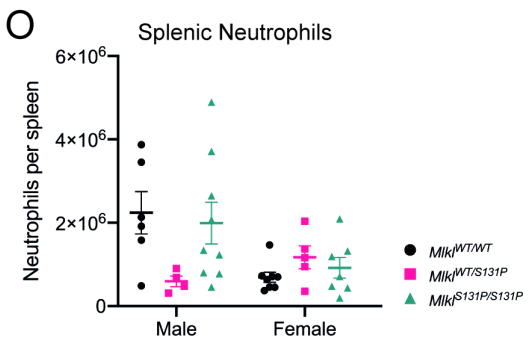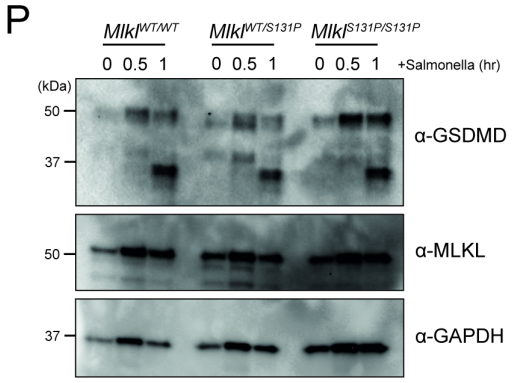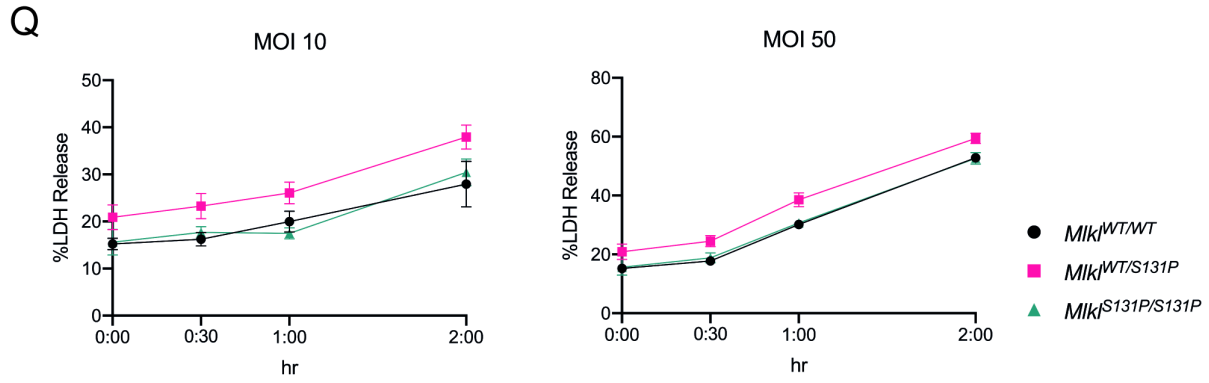
Supplementary Figure 5 cont.